ELSEVIER

Physica C 363 (2001) 260–284

PHYSICA C

www.elsevier.com/locate/physc

Analysis of the Knight shift data on Li and Zn substituted $YBa_2Cu_3O_{6+x}$

N. Bulut *

Department of Physics, Koç University, Sariyer, 80910 Istanbul, Turkey

Received 9 January 2001; accepted 9 May 2001

Abstract

The Knight shift data on Li and Zn substituted $YBa_2Cu_3O_{6+x}$ are analyzed using an itinerant model with short-range antiferromagnetic correlations. The model parameters, which are determined by fitting the experimental data on the transverse nuclear relaxation rate T_2^{-1} of pure $YBa_2Cu_3O_{6+x}$, are used to calculate the Knight shifts for various nuclei around a nonmagnetic impurity located in the CuO_2 planes. The calculations are carried out for Li and Zn impurities substituted into optimally doped and underdoped $YBa_2Cu_3O_{6+x}$. The results are compared with the ^{7}Li and ^{89}Y Knight shift measurements on these materials.

PACS: 74.62.Dh; 76.60.Cq; 71.10.Fd; 74.72.Bk
Keywords: Knight shift; Nonmagnetic impurities; Antiferromagnetic correlations; $YBa_2Cu_3O_{6+x}$

1. Introduction

The substitution of nonmagnetic impurities into cuprates serves as a probe of the electronic correlations in these materials. In particular, it has been found that the nonmagnetic impurities significantly influence the magnetic correlations in the normal state [1–10]. The ^{89}Y NMR experiments [1,4] find that when Zn is substituted into $YBa_2Cu_3O_{6+x}$, the Knight shifts of the Y sites near the impurity are strongly enhanced as the temperature is lowered. It has been also found that the Li impurities induce changes in the local magnetic environment similar to that of Zn [2]. A Curie-like T dependence is found in the SQUID measurements of the uniform susceptibility for Zn substituted $YBa_2Cu_3O_{6+x}$ [3] as well. It has been also shown that the Zn impurities induce a Curie-like T dependence in the broadening of the ^{63}Cu(2) spectral line in $YBa_2Cu_3O_{6.7}$ [7]. The effects of nonmagnetic impurities in $YBa_2Cu_3O_{6+x}$ have been also probed by the measurements of the ^{89}Y and ^{7}Li NMR relaxation rates T_1^{-1} [1,4,6] and by the inelastic neutron scattering experiments [11–14]. The T_1^{-1} measurements have been also carried out for Cu(2) in Zn substituted $YBa_2Cu_3O_7$ [8] and $YBa_2Cu_4O_8$ [9] systems. The effects of the nonmagnetic impurities on the magnetic correlations were also studied in $La_{1.85}Sr_{0.15}CuO_4$ with Al impurities [10].

Numerous theoretical studies [15–22] have been carried out for exploring the effects of the nonmagnetic impurities on the magnetic properties of the cuprates. The effects of a nonmagnetic impurity embedded into the two-dimensional (2D)

* Tel.: +90-212-338-1570; fax: +90-212-338-1559.
E-mail address: nbulut@ku.edu.tr (N. Bulut).

0921-4534/01/$ - see front matter
PII: S0921-4534(01)00755-9

Heisenberg lattice [15,16] as well as in gapped Heisenberg antiferromagnets [16] have been studied. The exact diagonalization calculations have been used to study the effects of a nonmagnetic impurity in the t–J model [17,18]. Theoretical studies have been also carried out for the underdoped $YBa_2Cu_3O_{6+x}$, where there is a spin pseudogap [19]. Calculations of the neutron scattering intensity for Zn substituted $YBa_2Cu_3O_{6+x}$ have been also carried out [20,22].

In this paper, a simple framework [21] of one nonmagnetic impurity embedded into the lattice of the 2D Hubbard model will be used to make comparisons with the ^{7}Li and ^{89}Y Knight shift measurements on the Li and Zn substituted $YBa_2Cu_3O_{6+x}$. The purpose of this paper is to study the effects of the nonmagnetic impurities on the magnetic correlations in the normal state of the cuprates. In the following, the 2D Hubbard model and the random-phase approximation (RPA) will be used for modeling the antiferromagnetic correlations in pure $YBa_2Cu_3O_{6+x}$. The 2D Hubbard model is defined by

$$H = -t\sum_{\langle i,j\rangle,\sigma}(c^{\dagger}_{i\sigma}c_{j\sigma} + c^{\dagger}_{j\sigma}c_{i\sigma}) + U\sum_i c^{\dagger}_{i\uparrow}c_{i\uparrow}c^{\dagger}_{i\downarrow}c_{i\downarrow} - \mu\sum_{i,\sigma}c^{\dagger}_{i\sigma}c_{i\sigma}. \quad (1)$$

Here $c_{i\sigma}$ ($c^{\dagger}_{i\sigma}$) annihilates (creates) an electron with spin σ at site i, t is the near-neighbor hopping matrix element, U is the onsite Coulomb repulsion, and μ is the chemical potential. The model parameters for the pure system will be determined by fitting the experimental data [23–26] on the transverse nuclear relaxation rate T_2^{-1} of pure $YBa_2Cu_3O_{6+x}$.

Next, a static extended impurity potential will be used to incorporate the effects of one nonmagnetic impurity embedded into the 2D Hubbard model. There is considerable support for using an extended impurity potential for modeling the effective impurity potential [27,28]. Here, it will be assumed that the effective interaction between an impurity located at site $\mathbf{r}_0$ and a quasiparticle at $\mathbf{r}$ can be approximated by the static potential

$$V_{\rm eff}(\mathbf{r}_0,\mathbf{r}) = V_0\delta(\mathbf{r}_0,\mathbf{r}) + V_1\sum_{\alpha=1}^{4}\delta(\mathbf{r},\mathbf{r}_0+\rho_\alpha), \quad (2)$$

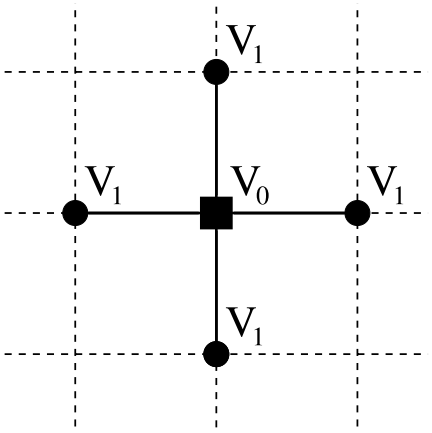

Fig. 1. Illustration of the extended impurity potential due to a nonmagnetic impurity represented by the filled square at the center. Here, V_0 is the onsite component of the impurity potential and V_1 acts at the nearest-neighbor sites of the impurity.

which has a range of one lattice spacing. In Eq. (2), α sums over the four near-neighbor sites of the impurity as illustrated in Fig. 1. Using this simple form of $V_{\rm eff}$, the Knight shift of various nuclei around the impurity will be calculated, and the results will be compared with the experimental data.

In the following, since the Zn and Li impurities are considered to have closed outer electronic shells with $S = 0$, the onsite component V_0 will be set to a large negative value. On the other hand, the near-neighbor component V_1 will be used as a free model parameter. Clearly, this form of $V_{\rm eff}$, Eq. (2), is a simple approximation. For instance, the range of $V_{\rm eff}$ could be more than one lattice spacing. Furthermore, $V_{\rm eff}$ could have scattering in the magnetic channel [29]. In fact, any magnetic scattering could drastically change the results presented here. Nevertheless, it is interesting to explore the consequences of this form of $V_{\rm eff}$ on the Knight shifts within this simple framework. Within this model at the level of RPA, the fitting of the ^{7}Li and ^{89}Y Knight shift data will require that V_1 is weakly attractive.

The comparisons will be first carried out with the ^{7}Li Knight shift, ^7K, measurements in Li substituted $YBa_2Cu_3O_{6.97}$ by Bobroff et al. [2]. Here, ^7K will be calculated for various values of V_1. It will be seen that the temperature dependence of

^{7}K can be fitted by using a $V_1 \approx -0.15t$. The effects of the nonmagnetic impurity on the ^{89}Y and the ^{63}Cu(2) Knight shifts for the sites near the impurity will also be given for this compound.

According to this simple model [21], the anomalous T dependence observed in the Knight shift data is due to the enhancement of the antiferromagnetic correlations in the local environment of the impurity. In this model, the scattering of the antiferromagnetic spin fluctuations by the impurity with large momentum transfers near $2\mathbf{k}_F$, where $\mathbf{k}_F$ is the Fermi wave vector, plays a particularly important role [21,22]. These scatterings locally enhance the antiferromagnetic correlations, and, in addition, allow for the Knight shift of the nuclear sites near the impurity to be coupled to the locally enhanced antiferromagnetic correlations.

Because of the presence of the spin pseudogap in underdoped $YBa_2Cu_3O_{6+x}$, it is indeed difficult to extend this analysis to this compound. However, the Knight shift experiments on underdoped $YBa_2Cu_3O_{6+x}$ yielded interesting results on the real-space structure of the induced magnetic correlations around the impurity. These measurements have been carried out for ^{7}Li in Li substituted $YBa_2Cu_3O_{6.6}$ [2] and for ^{89}Y in Zn or Li substituted $YBa_2Cu_3O_{6.64}$ [1,4]. For ^{89}Y, two magnetic resonance satellites in addition to the main line are found in the presence of the Zn or Li impurities in underdoped $YBa_2Cu_3O_{6+x}$. These satellites have been identified as belonging to the first and the second neighbor Y sites of the impurity. The availability of the Knight shift data on ^{7}Li and the two ^{89}Y satellites gives valuable information on the real-space structure of the magnetic correlations in the local environment of the impurity [4]. The ^{7}Li and ^{89}Y Knight shift measurements by Mahajan et al. [1,4] and the data on the Knight shift of ^{63}Cu(2), $^{63}K_c$, by Julien et al. [7] point out that a staggered polarization cloud forms around the impurity when a uniform magnetic field is applied. Hence, here, using simple assumptions, the results of the calculations will be compared with the ^{7}Li and ^{89}Y Knight shifts in order to see whether this simple model has some of the features observed experimentally. Results on $^{63}K_c$ will also be presented. It is important to keep in mind that the purpose in this paper will not be to present a theory of the magnetic correlations in the pseudogap state within the presence of nonmagnetic impurities. This is clearly beyond the simple model used here. Rather, the purpose is to study the real-space structure of the deformations induced by the impurity by making simple assumptions. It would have been more desirable to carry out such a study for optimally doped $YBa_2Cu_3O_7$, where this model is more applicable, but in that case the ^{89}Y lines are not resolved. Here, the model parameters determined by fitting the T_2^{-1} data on pure $YBa_2Cu_3O_{6.63}$ will be used to calculate the ^{7}Li and ^{89}Y Knight shifts. Initially, the Knight shifts will be calculated by neglecting the opening of the pseudogap in the $\mathbf{q} \to 0$ component of the magnetic susceptibility of the pure system. Even in this case, it will be found that for V_1 between $-0.125t$ and $-0.15t$, the real-space pattern of the magnetic correlations around the impurity is similar to what is seen experimentally. Later on, a pseudo gap in the $\mathbf{q} \to 0$ component of the magnetic susceptibility will be introduced artificially. In this case, comparisons with the data require $V_1 \approx -0.15t$. It has to be re-emphasized that the results on the underdoped $YBa_2Cu_3O_{6+x}$ needs to be interpreted cautiously. The treatment of the pseudogap is clearly not rigorous. An especially important point is that the presence of the pseudogap can introduce new physics which is quite different than the simple scenario discussed here using a weak-coupling model.

In Section 2 below, the model will be introduced. After comparisons with the experimental data in Sections 3.1 and 3.2, the pattern of the magnetic correlations around the impurity will be shown in Section 3.3. The implications of these calculations and the role of the antiferromagnetic correlations will be discussed in Section 4. In addition, here, the dependence of the results on the effective bandwidth will be studied, and the hyperfine couplings used in the calculations will be compared with the experimental estimates. In Section 5, the summary and the conclusions will be given.

2. Model

Here, the framework for calculating the Knight shifts will be introduced. In Section 2.1, the mod-

eling of the magnetic susceptibility for pure $YBa_2Cu_3O_{6+x}$ will be presented. The model parameters, which will be used to parameterize the antiferromagnetic correlations of pure $YBa_2Cu_3O_{6+x}$, will be determined by fitting the experimental data on the transverse nuclear relaxation rate T_2^{-1} of $YBa_2Cu_3O_{6+x}$ [23–26]. In Section 2.2, the static extended impurity potential used for approximating the interaction between the impurity and the electrons will be discussed. In the following section, the calculation of the magnetic susceptibility for the case of one impurity will be presented. In Section 2.4, the hyperfine interactions for the ^{7}Li and ^{89}Y nuclear spins will be introduced.

2.1. Parameterization of $\chi(\mathbf{q},\omega)$ for pure $YBa_2Cu_3O_{6+x}$

In this paper, it will be assumed that the magnetic correlations of pure $YBa_2Cu_3O_{6+x}$ can be approximated by the 2D Hubbard model. The magnetic susceptibility of the pure system is defined by

$$\chi_{\rm pure}(\mathbf{q}) = \int_0^\beta d\tau \langle m^-(\mathbf{q},\tau) m^+(\mathbf{q},0)\rangle. \tag{3}$$

Here, τ is the Matsubara time, $m^+(\mathbf{q},0) = N^{-1/2}\sum_{\mathbf{p}} c_{\mathbf{p}+\mathbf{q}\uparrow} c_{\mathbf{p}\downarrow}$, $m^-(\mathbf{q},\tau) = e^{H\tau} m^-(\mathbf{q},0) e^{-H\tau}$, and $m^-(\mathbf{q},0) = N^{-1/2}\sum_{\mathbf{p}} c_{\mathbf{p}+\mathbf{q}\downarrow} c_{\mathbf{p}\uparrow}$. The RPA from $\chi_{\rm pure}$ is

$$\chi_{\rm pure}(\mathbf{q}) = \frac{\chi_0^{\rm L}(\mathbf{q})}{1 - U\chi_0^{\rm L}(\mathbf{q})}. \tag{4}$$

Here, U is the renormalized Coulomb repulsion and the static Lindhard susceptibility $\chi_0^{\rm L}(\mathbf{q})$ is given by

$$\chi_0^{\rm L}(\mathbf{q}) = \frac{1}{N}\sum_{\mathbf{p}} \frac{f(\varepsilon_{\mathbf{p}+\mathbf{q}}) - f(\varepsilon_{\mathbf{p}})}{\varepsilon_{\mathbf{p}} - \varepsilon_{\mathbf{p}+\mathbf{q}}}, \tag{5}$$

where $f(\varepsilon_{\mathbf{p}})$ is the Fermi factor and $\varepsilon_{\mathbf{p}} = -2t \times (\cos p_x + \cos p_y) - \mu$. Using this form for $\chi_{\rm pure}(\mathbf{q})$ with the renormalized values of U and the hopping matrix element t, the longitudinal and the transverse relaxation rates T_1^{-1} and T_2^{-1} for $YBa_2Cu_3O_7$ have been calculated [30,31]. In this model, the renormalization of U is due to the particle–particle correlations and the single-particle self-energy corrections, and the renormalization of the bandwidth is due to the Coulomb correlations [32]. The value of U will be determined by fitting the experimental data on the ^{63}Cu(2) transverse relaxation rate T_2^{-1} in pure $YBa_2Cu_3O_{6+x}$. In the following, the effective bandwidth W will be taken to be 1 eV as in Refs. [30,31]. Later, in Section 4.3 the dependence of the results on W will be studied.

The transverse nuclear relation rate T_2^{-1} of ^{63}Cu(2) for an orienting field along the c-axis is given by [23]

$$\left(\frac{1}{T_2}\right)^2 = \frac{0.69}{32\hbar^2}\left\{\frac{1}{N}\sum_{\mathbf{q}} |A(\mathbf{q})|^4 \chi_{\rm pure}^2(\mathbf{q}) - \left(\frac{1}{N}\sum_{\mathbf{q}} |A(\mathbf{q})|^2 \chi_{\rm pure}(\mathbf{q})\right)^2\right\}, \tag{6}$$

where

$$A(\mathbf{q}) = A_{\rm c} + 2B(\cos q_x + \cos q_y). \tag{7}$$

Here, the following hyperfine interaction [33] has been assumed for the ^{63}Cu nuclear spin at site i,

$$\sum_{\alpha=x,y,z} A_{\alpha\alpha} I_i^\alpha S_i^\alpha + B\sum_{\delta=1}^{4} \mathbf{I}_i \cdot \mathbf{S}_{i+\delta}, \tag{8}$$

where δ sums over the four nearest-neighbors of site i. For the hyperfine couplings, $A_{\rm c} = -4B = -2.45\times 10^{-18}$ erg, corresponding to 164 kOe/$\mu_{\rm B}$, will be used as in Ref. [31]. In fitting the T dependence of T_2^{-1} with the RPA form of Eq. (4), U will be adjusted as T is varied. Clearly, this is a simple, approximate procedure for determining the strength of the antiferromagnetic correlations in the pure system. In fact, the model is so simple that electron filling $\langle n\rangle$ will be taken to be 0.86 for both the underdoped and optimally doped systems. Hence, the only feature which differentiates between the underdoped and the optimally doped systems in this model is the strength of the antiferromagnetic correlations of the pure system which is set by adjusting U to fit the T_2^{-1} data. As discussed in Ref. [21], the antiferromagnetic correlations of the impure system can get significantly enhanced by the impurity scattering as compared to those in the pure system.

The fitting of T_2^{-1} will be first carried out for optimally doped $YBa_2Cu_3O_{6+x}$. The transverse relaxation rate T_2^{-1} of $^{63}Cu(2)$ has been measured by Pennington and Slichter [23] in $YBa_2Cu_3O_7$, and by Imai et al. [25] in $YBa_2Cu_3O_{6.9}$. The data by Imai et al. [25] are represented by the open circles in Fig. 2(a). Here, it is seen that T_2^{-1} increases linearly as T is lowered from 300 to 100 K. The dashed line in this figure has been obtained by using the RPA form of Eq. (4) in Eq. (6) and by adjusting U to fit the experimental data. The resultant values of $U(T)$ are given by the dashed line in Fig. 2(b). Here one observes that as T is lowered from 300 to 100 K, $U(T)$ decreases by 5%. Note also that the dashed curve in Fig. 2(a) has been extrapolated up to 400 K, since in Section 3 the Knight shifts will be calculated up to this temperature.

The filled circles in Fig. 2(b) represent the T_2^{-1} data for $^{63}Cu(2)$ in $YBa_2Cu_3O_{6.63}$ measured by Takigawa [26]. Here it is seen that T_2^{-1} varies almost linearly for T between 160 and 300 K. Below 160 K, T_2^{-1} saturates. Because of this, the fitting of T_2^{-1} for $T < 160$ K will require more attention. This saturation might be due to two reasons: (1) the suppression of $\chi_{\text{pure}}(\mathbf{q} \sim 0)$ because of the opening of the magnetic pseudogap, or (2) the saturation of $\chi_{\text{pure}}(\mathbf{q})$ for $\mathbf{q} \sim (\pi, \pi)$. In the first case, $\chi_{\text{pure}}(\mathbf{q} \sim (\pi, \pi))$ would continue to increase as T is lowered and the saturation of T_2^{-1} would be due directly to the suppression of $\chi_{\text{pure}}(\mathbf{q} \sim 0)$. In the other case, the saturation of T_2^{-1} would be due to the saturation of the antiferromagnetic correlations. In order to take into account these two possibilities, the fitting of T_2^{-1} below 160 K will be done in two ways. In the first case, the saturation of T_2^{-1} will be attributed to the suppression of $\chi_{\text{pure}}(\mathbf{q} \sim 0)$ and it will be assumed that without this effect T_2^{-1} would have continued to increase linearly as T is lowered below 160 K. Hence, in this case, T_2^{-1} will be extrapolated for $T < 160$ K as shown by the solid line in Fig. 2(a). The resultant values of $U(T)$ are shown by the solid curve in Fig. 2(b). In the second case, the T_2^{-1} data below 160 K will be fitted directly as shown by the dotted curve in Fig. 2(a). The resultant $U(T)$ is shown by the dotted curve in Fig. 2(b). By comparing the solid and the dotted curves for $T < 160$ K in Fig. 2(a) and (b), it is seen that small changes in U produce significant changes in T_2^{-1}. This is because the system is close to a magnetic instability with a large Stoner enhancement for $\mathbf{q} \sim (\pi, \pi)$.

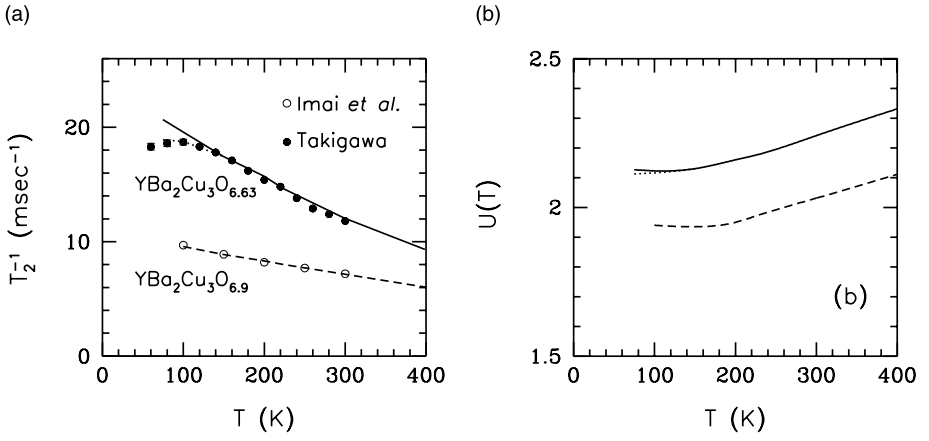

Fig. 2. (a) Transverse nuclear relaxation rate T_2^{-1} for $^{63}Cu(2)$ versus T in pure $YBa_2Cu_3O_{6+x}$. The open and the filled circles represent the experimental data by Imai et al. [25] and Takigawa [26] for $YBa_2Cu_3O_{6.9}$ and for $YBa_2Cu_3O_{6.63}$, respectively. The dashed line is a fit of the T_2^{-1} data by Imai et al. [25] on $YBa_2Cu_3O_{6.9}$. For $YBa_2Cu_3O_{6.63}$, the fitting of the data below 160 K has been carried out in two ways. The solid line has been obtained by ignoring the saturation of T_2^{-1} below ~160 K, and the dotted curve has been obtained by fitting the data for $80 < T < 160$ K. (b) Temperature dependence of U. The dashed curve has been obtained by fitting the T_2^{-1} measurements on pure $YBa_2Cu_3O_{6.9}$. The solid and the dotted curves have been obtained for pure $YBa_2Cu_3O_{6.63}$ by fitting the solid and the dotted curves seen in (a).

At this point, it is useful to see the strength of the antiferromagnetic correlations required for fitting the T_2^{-1} data. The dashed curve in Fig. 3(a) shows $\chi_{\rm pure}(\mathbf{q})$ versus $\mathbf{q}$ obtained by fitting the T_2^{-1} data on pure $YBa_2Cu_3O_{6.9}$ at 100 K. The solid and the dotted curves represent $\chi_{\rm pure}(\mathbf{q})$ obtained with the first and the second scenarios, respectively, for fitting T_2^{-1} of $YBa_2Cu_3O_{6.63}$ at 100 K [26]. For the form of $\chi_{\rm pure}(\mathbf{q})$ used here, Eqs. (4) and (5), the peak in $\chi_{\rm pure}(\mathbf{q})$ occurs at an incommensurate wave vector $\mathbf{Q}^*$ away from $\mathbf{Q}=(\pi,\pi)$. The neutron scattering experiments [34,35] on $YBa_2Cu_3O_{6+x}$ find that in the superconducting state, the spin-fluctuation spectral weight $\mathrm{Im}\,\chi_{\rm pure}(\mathbf{q},\omega)$ peaks away from (π,π), but with an incommensuration which is more than what is observed in Fig. 3(a). The form of $\chi_{\rm pure}(\mathbf{q})$ used here is clearly a crude approximation. The results shown below will not depend sensitively on the amount of the incommensuration, rather they will depend on the total integrated weight in the $\mathbf{q}\sim(\pi,\pi)$ region of the $\mathbf{q}$-space. Further results on the nature of the antiferromagnetic correlations are shown in Fig. 3(b). The dashed line in Fig. 3(b) shows $\chi_{\rm pure}(\mathbf{Q}^*)$

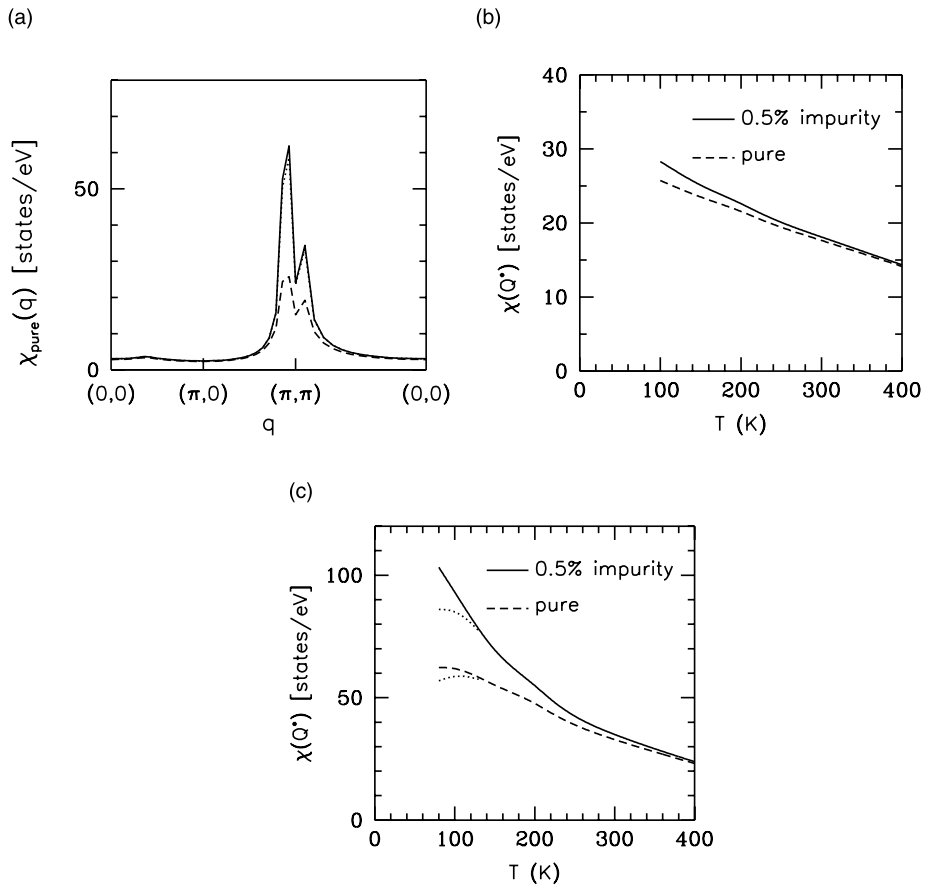

Fig. 3. (a) $\chi_{\rm pure}(\mathbf{q})$ versus $\mathbf{q}$ at 100 K for the pure system. The dashed curve represents results for optimally doped $YBa_2Cu_3O_{6+x}$. The solid and the dotted curves have been obtained for underdoped $YBa_2Cu_3O_{6+x}$. (b) $\chi(\mathbf{Q}^*)$ versus T for optimally doped $YBa_2Cu_3O_{6+x}$, where $\mathbf{Q}^*$ is the wave vector at which $\chi(\mathbf{q})$ peaks at low temperatures. Here, the dashed curve is for optimally doped pure $YBa_2Cu_3O_{6+x}$, and the solid curve is for the case of 0.5% dilute impurities. (c) $\chi(\mathbf{Q}^*)$ versus T for underdoped $YBa_2Cu_3O_{6+x}$. The dashed curve is for the pure system and the solid curve is for the case with 0.5% impurities. The dotted curves were obtained by using the values of U given by the dotted curves in Fig. 2(b). The results for the impure systems shown in (b) and (c) were calculated for $V_1=-0.15t$ as described in Section 4.1.

versus T for optimally doped $YBa_2Cu_3O_{6+x}$. Also shown in this figure by the solid line are the results for $\chi(\mathbf{Q}^*)$ of the impure system with 0.5% randomly distributed impurities which will be discussed below in Section 4.1. Fig. 3(c) shows similar results for $\chi(\mathbf{Q}^*)$ of underdoped $YBa_2Cu_3O_{6+x}$. Here, it is seen that $\chi(\mathbf{Q}^*)$ gets significantly enhanced by the substitution of the nonmagnetic impurities, especially for underdoped $YBa_2Cu_3O_{6+x}$. By comparing Fig. 2(a) with Fig. 3(b) and (c), it is also seen that the temperature dependence of T_2^{-1} and $\chi_{\text{pure}}(\mathbf{Q}^*)$ are closely related, as expected.

2.2. Effective impurity potential

The effects of one nonmagnetic impurity located at site $\mathbf{r}_0$ will be taken into account by adding to Eq. (1) the term

$$\sum_{i,\sigma} V_{\text{eff}}(\mathbf{r}_0,\mathbf{r}_i)c^\dagger_{i\sigma}c_{i\sigma}, \tag{9}$$

where $V_{\text{eff}}(\mathbf{r}_0,\mathbf{r})$ is given by Eq. (2). The importance of using an extended impurity potential has been previously noted [27,28]. In Ref. [28], it has been pointed out that the Coulomb correlations of the host could cause the extended nature of the effective interaction. The fact that the defects generated by the electron irradiation of the samples have similar effects on the T_c suppression [36] and on the magnetic properties [37] also supports using an impurity potential with only a potential scattering term.

In the following, the onsite component of the impurity potential, V_0, will be set to a large negative value, $-100t$, in order to model the closed electronic shell of the nonmagnetic impurity. As long as $|V_0|$ has a large value, its exact magnitude or its sign does not play an important role. For instance, using $V_0 = -200t$ instead of $-100t$ does not change the results. The near-neighbor component V_1, on the other hand, will be used as a free parameter in fitting the Knight shift measurements on Li and Zn substituted $YBa_2Cu_3O_{6+x}$. In the next section, the effects of this static extended impurity potential on the magnetic susceptibility will be calculated.

2.3. Magnetic susceptibility within the presence of one nonmagnetic impurity

The calculation of χ within the presence of a nonmagnetic impurity used here follows that given in Ref. [21]. First, the effects of the impurity on the single-particle Green's function will be calculated. The single-particle Green's function in Matsubara frequency space is defined by

$$G(\mathbf{r}_i,\mathbf{r}_j,\mathrm{i}\omega_n) = -\int_0^\beta \mathrm{d}\tau\, \mathrm{e}^{\mathrm{i}\omega_n\tau}\langle c_{i\sigma}(\tau)c^\dagger_{j\sigma}(0)\rangle, \tag{10}$$

where $\omega_n = (2n+1)\pi T$. For the pure system with $U = 0$, one has

$$G_0(\mathbf{r}_i,\mathbf{r}_j,\mathrm{i}\omega_n) = \frac{1}{N}\sum_{\mathbf{p}} \mathrm{e}^{\mathrm{i}\mathbf{p}\cdot(\mathbf{r}_i-\mathbf{r}_j)}G_0(\mathbf{p},\mathrm{i}\omega_n), \tag{11}$$

where

$$G_0(\mathbf{p},\mathrm{i}\omega_n) = \frac{1}{\mathrm{i}\omega_n - \varepsilon_{\mathbf{p}}}. \tag{12}$$

If an impurity is introduced at site $\mathbf{r}_0$, then one gets

$$G(\mathbf{r},\mathbf{r}',\mathrm{i}\omega_n) = G_0(\mathbf{r},\mathbf{r}',\mathrm{i}\omega_n) + \sum_{\mathbf{r}'',\mathbf{r}'''} G_0(\mathbf{r},\mathbf{r}'',\mathrm{i}\omega_n) \times T(\mathbf{r}'',\mathbf{r}''',\mathrm{i}\omega_n)G(\mathbf{r}''',\mathbf{r}',\mathrm{i}\omega_n), \tag{13}$$

where the T-matrix for the impurity scattering is given by

$$T(\mathbf{r},\mathbf{r}',\mathrm{i}\omega_n) = \delta(\mathbf{r},\mathbf{r}')V_{\text{eff}}(\mathbf{r}_0,\mathbf{r}) + \sum_{\mathbf{r}''} V_{\text{eff}}(\mathbf{r}_0,\mathbf{r}) \times G_0(\mathbf{r},\mathbf{r}'',\mathrm{i}\omega_n)T(\mathbf{r}'',\mathbf{r}',\mathrm{i}\omega_n). \tag{14}$$

The calculation of $G(\mathbf{r},\mathbf{r}',\mathrm{i}\omega_n)$ is illustrated diagrammatically in Fig. 4(a).

When the translational invariance is broken, the magnetic susceptibility is defined in real space as

$$\chi(\mathbf{r},\mathbf{r}',\mathrm{i}\omega_m) = \int_0^\beta \mathrm{d}\tau\, \mathrm{e}^{\mathrm{i}\omega_m\tau}\langle m^-(\mathbf{r},\tau)m^+(\mathbf{r}',0)\rangle, \tag{15}$$

where $m^+(\mathbf{r}) = c^\dagger_{\mathbf{r}\uparrow}c_{\mathbf{r}\downarrow}$, and $m^-(\mathbf{r}) = c^\dagger_{\mathbf{r}\downarrow}c_{\mathbf{r}\uparrow}$. The effects of a single impurity will be first calculated for $U = 0$, giving the irreducible susceptibility $\chi_0(\mathbf{r},\mathbf{r}',\mathrm{i}\omega_m)$, and then the effects of the Coulomb correlations will be included. The diagrams representing the effects of the impurity on χ_0 are shown in Fig. 4(b) and (c). Both the self-energy and the vertex

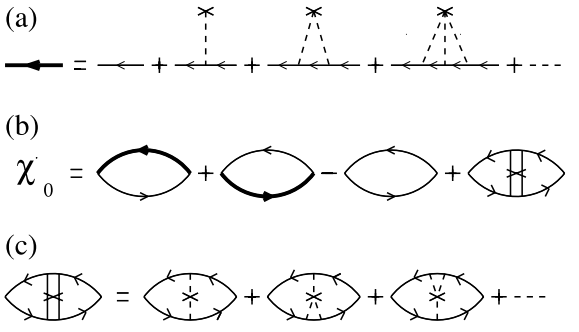

Fig. 4. Feynman diagrams for (a) the dressed single-particle Green's function G and (b, c) the irreducible susceptibility χ_0 within the presence of one impurity.

corrections need to be included [38], and the resulting expression for $\chi_0(\mathbf{r},\mathbf{r}',i\omega_m)$ is given by

$$\begin{aligned}\chi_0(\mathbf{r},\mathbf{r}',i\omega_m) &= -T\sum_{i\omega_n}\Big\{[G(\mathbf{r},\mathbf{r}',i\omega_n+i\omega_m)G_0(\mathbf{r}',\mathbf{r},i\omega_n)\\ &+ G_0(\mathbf{r},\mathbf{r}',i\omega_n+i\omega_m)G(\mathbf{r}',\mathbf{r},i\omega_n)\\ &- G_0(\mathbf{r},\mathbf{r}',i\omega_n+i\omega_m)G_0(\mathbf{r}',\mathbf{r},i\omega_n)]\\ &+ \sum_{\mathbf{r}_1,\mathbf{r}_2,\mathbf{r}_3,\mathbf{r}_4} G_0(\mathbf{r},\mathbf{r}_1,i\omega_n+i\omega_m)\\ &\times G_0(\mathbf{r}_2,\mathbf{r}',i\omega_n+i\omega_m)T(\mathbf{r}_1,\mathbf{r}_2,i\omega_n+i\omega_m)\\ &\times T(\mathbf{r}_3,\mathbf{r}_4,i\omega_n)G_0(\mathbf{r}_3,\mathbf{r},i\omega_n)G_0(\mathbf{r}',\mathbf{r}_4,i\omega_n)\Big\}.\end{aligned} \tag{16}$$

Note that the irreducible impurity-scattering vertex has been used in calculating the vertex corrections to χ_0 instead of the reducible one. This is necessary in order to prevent double counting, since here the effects of only one impurity are calculated.

Next, the Coulomb correlations are included by solving the RPA equation

$$\begin{aligned}\chi(\mathbf{r},\mathbf{r}',i\omega_m) &= \chi_0(\mathbf{r},\mathbf{r}',i\omega_m)\\ &+ U\sum_{\mathbf{r}''}\chi_0(\mathbf{r},\mathbf{r}'',i\omega_m)\chi(\mathbf{r}'',\mathbf{r}',i\omega_m)\end{aligned} \tag{17}$$

for $\chi(\mathbf{r},\mathbf{r}',i\omega_m)$. Here χ is calculated for an N-site square lattice with one nonmagnetic impurity located at the center using periodic boundary conditions. The calculations are carried out on sufficiently large lattices so that the finite size effects are small. In Ref. [21], the finite size effects on χ have been studied in detail.

The Knight shift is determined by $\chi(\mathbf{r},\mathbf{r}') = \chi(\mathbf{r},\mathbf{r}',i\omega_m=0)$. In the following section, the hyperfine interactions, which relate $\chi(\mathbf{r},\mathbf{r}')$ to the Knight shifts, will be discussed for ^{7}Li and ^{89}Y.

2.4. Hyperfine interactions for ^{7}Li and ^{89}Y

The hyperfine interaction between the ^{7}Li nuclear spin with $^7I = 3/2$ substituted into a Cu(2) site and the electronic spins will be modeled by the following hyperfine coupling [2]

$$C\sum_{\delta=1}^{4} {}^7\mathbf{I}\cdot\mathbf{S}_\delta. \tag{18}$$

Here δ sums over the four Cu(2) sites neighboring the Li impurity. The nature of this interaction is similar to that of the transferred hyperfine coupling of the ^{63}Cu(2) nuclear spins to the electronic spins at the neighboring Cu(2) sites given by the second term in Eq. (8) [33]. In Section 3, the magnitude of the ^{7}Li hyperfine coupling C will be taken to be 1.8×10^{-20} erg, corresponding to 0.85 kOe/μ_B. This choice for the value of C will be discussed later in Section 4.3. As a result of this coupling, Eq. (18), the Knight shift of ^{7}Li is (see Appendix A)

$${}^7K = \frac{1}{2}\left(\frac{\gamma_e}{{}^7\gamma_n}\right)C4k(\mathbf{r}=(1,0)), \tag{19}$$

where $k(\mathbf{r})$ is defined by

$$k(\mathbf{r}) = \sum_{\mathbf{r}'}\chi(\mathbf{r},\mathbf{r}'), \tag{20}$$

and γ_e and $^7\gamma_n$ are the gyromagnetic ratios of the electron and the ^{7}Li nuclear spin. The factor of four in Eq. (19) is because the Li impurity has four Cu(2) neighbors.

The hyperfine interaction for the ^{89}Y nuclear spin with $^{89}I = 1/2$ is

$$D\sum_{\alpha=1}^{8} {}^{89}\mathbf{I}\cdot\mathbf{S}_\alpha, \tag{21}$$

where α sums over the eight Cu(2) sites neighboring the ^{89}Y nuclear spin. In Section 3, the hyperfine interaction D will be assumed to be -2.2×10^{-20} erg, corresponding to -1.0 kOe/μ_B, in order to fit the normal state value of ^{89}K in pure $YBa_2Cu_3O_{6+x}$ using a bandwidth of $W=1$ eV. Later in Section 4.3, the dependence of the results on W and on the values of the hyperfine couplings C and D will be discussed. Here, it will also be assumed that the ^{89}Y hyperfine couplings do not change upon the substitution of the nonmagnetic impurity. Then the Knight shift for ^{89}Y at a particular Y lattice site is given by

$$^{89}K=\frac{1}{2}\left(\frac{\gamma_e}{^{89}\gamma_n}\right)D\sum_{\alpha=1}^{8}k(\mathbf{r}_\alpha), \tag{22}$$

where $\mathbf{r}_\alpha$ are the locations of the eight nearest-neighbor Cu(2) sites of the Y site in the CuO_2 bilayer. For dilute Li or Zn impurities, the ^{89}Y nuclear spin will be affected by an impurity located in one of the layers of the CuO_2 bilayer in $YBa_2Cu_3O_{6+x}$. Here, it will be assumed that the changes induced in ^{89}K are due only to the changes in the magnetic correlations in the layer which contains the impurity as it was done in Ref. [4]. Also, in the following, the quantity of interest for ^{89}Y will be the change in the Knight shift of ^{89}Y due to the presence of the impurity. Hence, the calculations will be carried out for

$$\delta^{89}K=\frac{1}{2}\left(\frac{\gamma_e}{^{89}\gamma_n}\right)D\left[\sum_{\alpha=1}^{4}k(\mathbf{r}_\alpha)-4\chi_{\text{pure}}\right], \tag{23}$$

where α sums over the four Cu(2) sites neighboring the impurity in the layer which contains the impurity. In Eq. (23), χ_{pure} is the uniform static susceptibility of the pure system. The value of ^{89}K will depend strongly on the location of the ^{89}Y nuclear spin with respect to the impurity. In Fig. 5, a sketch of the various Y sites with respect to the impurity site is given. Note that the measurement of ^{89}K at the Y sites near the impurity, along with that of ^{7}K, determines the real-space structure of $k(\mathbf{r})$ in the environment of the impurity. For instance, ^{89}K for Y(1) is determined by $k(\mathbf{r}=(1,0))$ and $k(\mathbf{r}=(1,1))$, while ^{7}K is set by $k(\mathbf{r}=(1,0))$. In Section 3, the results of the calculations on ^{7}K and ^{89}K for various Y sites will be shown and compared with the experimental data.

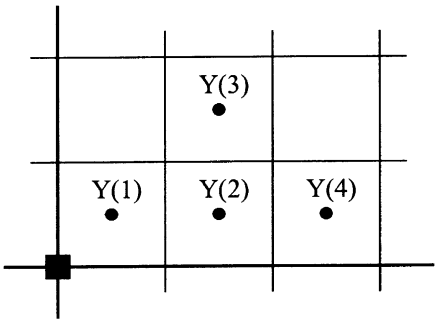

Fig. 5. Sketch of the neighboring Y(i) sites of a nonmagnetic impurity located in the CuO_2 plane. Here, the filled square indicates the impurity site.

3. Results of calculations

The comparison of the results with the experimental data will be carried out first for the optimally doped and then for the underdoped $YBa_2Cu_3O_{6+x}$.

3.1. Results on optimally doped $YBa_2Cu_3O_{6+x}$

The filled circles in Fig. 6(a) denote the experimental data by Bobroff et al. [2] on the ^{7}Li Knight shift ^{7}K for $YBa_2Cu_3O_{6.97}$ with dilute Li impurities. The curves in this figure represent the results of the calculations of ^{7}K for various values of V_1 as indicated next to the curves. The model parameters other than V_1 were already set by fitting the T_2^{-1} data on pure $YBa_2Cu_3O_{6.9}$ by Imai et al. [25] as discussed in Section 2.1. Here, it is seen that for $V_1\approx-0.15t$ the calculated values of ^{7}K are in agreement with the experimental data. It is useful to compare these results with what is expected for the ^{7}Li Knight shift if the magnetic correlations had not changed upon the substitution of the impurity and had remained the same as in the pure material. In Fig. 6(b), $^{7}K_0$ defined by

$$^{7}K_0=\frac{1}{2}\left(\frac{\gamma_e}{^{7}\gamma_n}\right)C4\chi_{\text{pure}}, \tag{24}$$

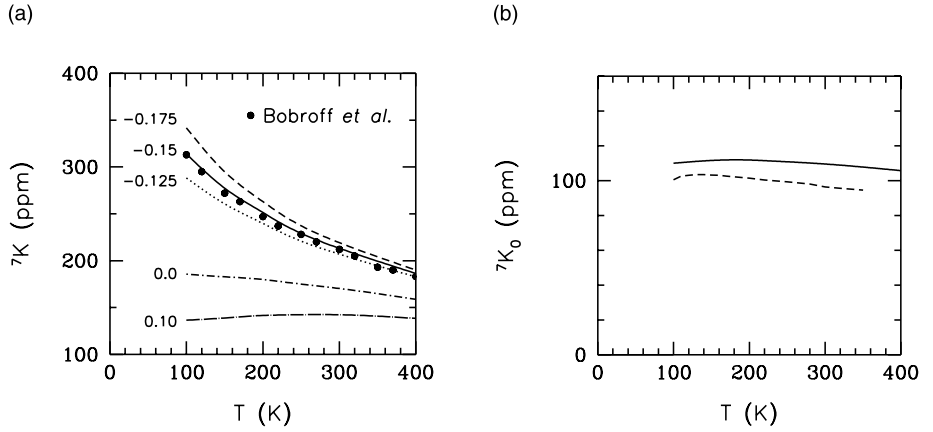

Fig. 6. (a) ^{7}Li Knight shift ^7K versus T in optimally doped $YBa_2Cu_3O_{6+x}$. The filled circles represent the Knight shift data by Bobroff et al. [2]. The curves represent the results of the calculations for various values of V_1/t which are indicated next to the curves. (b) Estimated temperature dependence of $^7K_0$ for optimally doped $YBa_2Cu_3O_{6+x}$. Here, $^7K_0$ represents the value of the ^{7}Li Knight shift, if the substitution of the Li impurity had not induced any changes in the magnetic correlations around it. The dashed curve is the experimental estimate of $^7K_0$ obtained by using the ^{89}K data [39] on pure optimally doped $YBa_2Cu_3O_{6+x}$. The solid line is the result obtained by setting $V_0 = V_1 = 0$ in this model.

where χ_{pure} is the uniform susceptibility of the pure system, is plotted as a function of the temperature. The solid line has been obtained from $\chi_{\text{pure}}(\mathbf{q} \to 0)$ given by Eq. (4) for optimally doped $YBa_2Cu_3O_{6+x}$. The dashed line in Fig. 6(b) has been obtained by rescaling the ^{89}Y Knight shift ^{89}K of pure $YBa_2Cu_3O_7$ [39] with

$$^7K_0 = \frac{1}{2}\left(\frac{^{89}\gamma_n C}{^7\gamma_n D}\right)^{89}K. \tag{25}$$

The factor of $1/2$ in this expression is because Y has eight Cu(2) near neighbors while Li has four. In these figures, it is also seen that for $V_1 = 0$, corresponding to an onsite impurity potential in the unitary limit, ^7K is enhanced with respect to $^7K_0$ but this enhancement is not sufficient to explain the experimental data. If positive values of V_1 are used, then ^7K gets suppressed with respect to the $V_1 = 0$ case.

The stoichiometry of the samples is a factor which could affect the comparisons with the data. Note that $U(T)$ used in calculating ^7K for $YBa_2Cu_3O_{6.97}$ was determined by fitting the T_2^{-1} data on $YBa_2Cu_3O_{6.9}$. For $YBa_2Cu_3O_7$, T_2^{-1} was measured at 100 K, and its value is 7.7 ± 0.6 ms^{-1} compared to $\sim$9.5 ms^{-1} for $YBa_2Cu_3O_{6.9}$. The value of 7.7 ms^{-1} for T_2^{-1} requires a slightly smaller value for U and, consequently, the fitting of ^7K is done using larger values of V_1. If one assumes that the T dependence of T_2^{-1} is given by a line which passes through 7.7 ms^{-1} at 100 K and which is parallel to the dashed line in Fig. 2(a), then the ^7K data can be fitted by using $V_1 \approx -0.275t$.

Based on these results and considering the simplicity of the model, the conclusions which can be reached are limited. Probably, the best thing to say is that the analysis of the ^7K data on optimally doped $YBa_2Cu_3O_{6+x}$ within this model at the level of RPA requires an impurity potential which is weakly attractive at the nearest-neighbor Cu(2) sites.

The results of the calculations for ^{89}K are shown in Fig. 7(a). Here, the temperature dependence of $\delta^{89}K$ is shown for the first four nearest-neighbor Y sites which are indicated in Fig. 5. In obtaining these results, $V_1 = -0.15t$ was used. Note that in Fig. 7(a) the expected values of the Knight shifts are close to each other. Experimentally, for optimally doped $YBa_2Cu_3O_{6+x}$, the expected resonance lines for the ^{89}Y nuclei near the Zn impurity are not resolved.

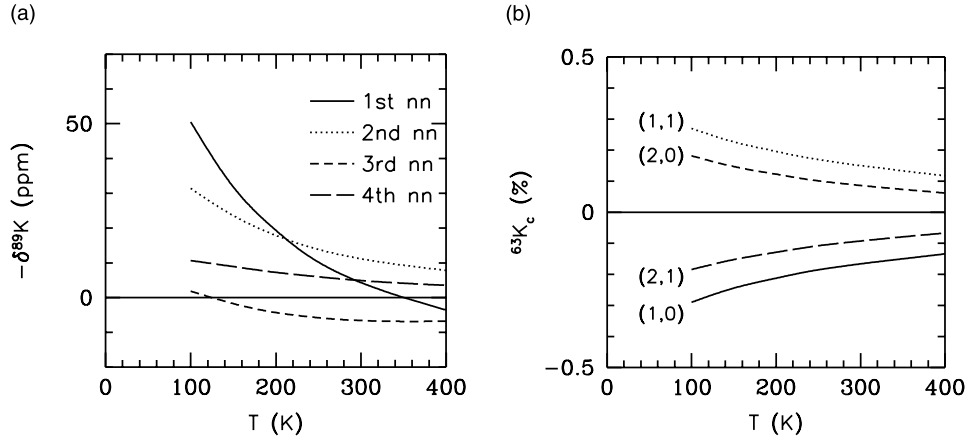

Fig. 7. (a) Temperature dependence of $-\delta^{89}K$ at the sites which are the first, second, third and the fourth nearest ^{89}Y neighbors of the impurity in optimally doped $YBa_2Cu_3O_{6+x}$. Here, $\delta^{89}K$ is the induced change in the ^{89}Y Knight shift up on the substitution of the impurity. (b) Temperature dependence of the ^{63}Cu(2) Knight shift for $\mathbf{H}\|c$, $^{63}K_c(\mathbf{r}_i)$, at various sites $\mathbf{r}_i$, which are indicated next to the curves, for the optimally doped $YBa_2Cu_3O_{6+x}$. The results shown in (a) and (b) were obtained by using $V_1 = -0.15t$.

Next, results on how the nonmagnetic impurity affects the ^{63}Cu(2) Knight shifts in this model are presented. The ^{63}Cu(2) Knight shift at site $\mathbf{r}_i$ with the orienting magnetic field $\mathbf{H}\|c$ is given by

$$^{63}K_c(\mathbf{r}_i) = \frac{1}{2}\left(\frac{\gamma_e}{^{63}\gamma_n}\right)\left[A_c k(\mathbf{r}_i) + B\sum_{\alpha=1}^{4} k(\mathbf{r}_\alpha)\right], \qquad (26)$$

where α sums over the four Cu(2) neighbors of $\mathbf{r}_i$. Fig. 7(b) shows the T dependence of $^{63}K_c(\mathbf{r}_i)$ for $V_1 = -0.15t$ for the first four neighboring Cu(2) sites of the impurity, which correspond to $\mathbf{r}_i = (1,0)$, $(1,1)$, $(2,0)$, and $(2,1)$. For the pure system, $^{63}K_c$ vanishes since $A_c + 4B = 0$. Here, it is seen that $^{63}K_c$ has a staggered pattern; it is negative at the sublattice of the $(1,0)$ site and it is positive at the sublattice of the impurity. This spatial pattern of $^{63}K_c(\mathbf{r}_i)$ is due to the staggered pattern of $k(\mathbf{r})$, which will be discussed in Sections 3.3 and 4.1. The measurements of $^{63}K_c$ have been carried out in $YBa_2Cu_3O_{6.7}$ by Julien et al. [7]. While the individual ^{63}Cu(2) lines are not resolved, it has been observed that the broadening of the linewidth has a Curie-like T dependence. This has been attributed to the development of a staggered polarization cloud around the impurity [7].

3.2. Results on underdoped $YBa_2Cu_3O_{6+x}$

The analysis of the Knight shift data on the underdoped $YBa_2Cu_3O_{6+x}$ is considerably more complicated because of the magnetic pseudogap. This is so because the origin of the magnetic pseudogap in this material is currently an unresolved issue. Hence, it is necessary to note that the purpose here is not to develop a theory for the magnetic susceptibility of the underdoped $YBa_2Cu_3O_{6+x}$ with impurities. Instead, the purpose is to explore any possible role of the antiferromagnetic correlations in producing the anomalous T dependence of the Knight shift data in underdoped $YBa_2Cu_3O_{6+x}$ within the presence of nonmagnetic impurities. The emphasis here will be on the real-space structure of the magnetic correlations around the impurity.

The ^{7}Li Knight shift measurements by Bobroff et al. [2] on underdoped $YBa_2Cu_3O_{6+x}$ with Li impurities found that ^7K increases rapidly as T is lowered. In Fig. 8(a), the experimental data on δ^7K defined by

$$\delta^7K = {}^7K - {}^7K_0 \qquad (27)$$

are compared with the results of the calculations. The comparisons are carried out for δ^7K rather

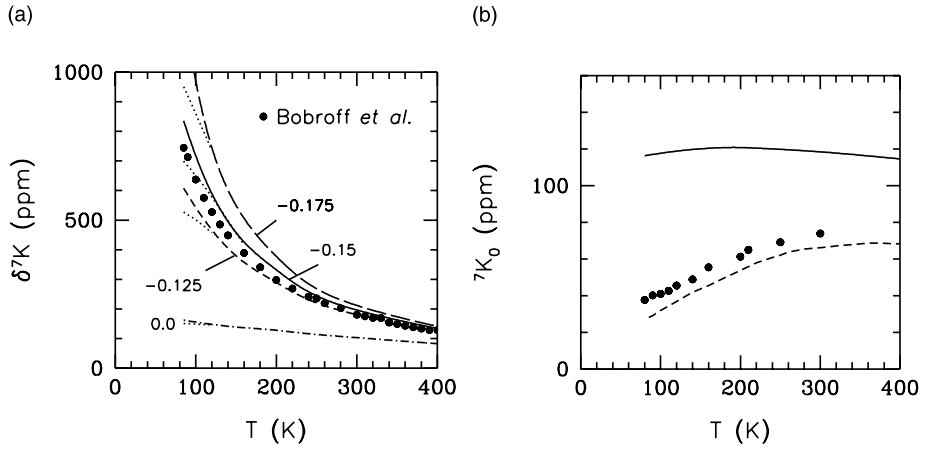

Fig. 8. (a) Temperature dependence of δ^7K for underdoped $YBa_2Cu_3O_{6+x}$. Here, δ^7K is defined as $^7K - {}^7K_0$, where ^7K is the ^{7}Li Knight shift and $^7K_0$ represents the value of the ^{7}Li Knight shift, if the substitution of the Li impurity had not changed the magnetic correlations around it. The filled circles represent the data by Bobroff et al. [2] on $YBa_2Cu_3O_{6.6}$. The curves represent the results of the calculations for various values of V_1/t which are indicated next to the curves. (b) Temperature dependence of $^7K_0$ for underdoped $YBa_2Cu_3O_{6+x}$. The solid points have been obtained by using the ^{89}K (main) data on underdoped $YBa_2Cu_3O_{6+x}$ with Zn impurities [1,4], while the dashed curve has been obtained by using the ^{89}K data on pure underdoped $YBa_2Cu_3O_{6+x}$ [39]. The solid curve shows the results of the calculations for $V_0 = V_1 = 0$.

than for ^7K in order to compensate for the effect of the magnetic pseudogap which is not taken into account here. The data points shown by the filled circles in Fig. 8(a) were obtained by subtracting from the ^7K data of Bobroff et al. [2] the quantity

$$^7K_0 = \frac{1}{2}\left(\frac{^{89}\gamma_n C}{^7\gamma_n D}\right)^{89}K \text{ (main)}, \tag{28}$$

where ^{89}K (main) is the Knight shift of the main ^{89}Y spectral line measured by Mahajan et al. [4] in Zn substituted $YBa_2Cu_3O_{6.6}$. The solid points in Fig. 8(b) indicate $^7K_0$ estimated this way. The dashed curve in Fig. 8(b) shows the estimate for $^7K_0$ obtained by using the ^{89}K measurements on pure $YBa_2Cu_3O_{6.63}$ [39]. In the Zn substituted samples, ^{89}K (main) is slightly shifted with respect to ^{89}K of the pure samples. This might be due to the difference in the stoichiometry of the Zn substituted and the pure samples, as discussed in Ref. [4].

The results of the calculations on δ^7K are represented by the various curves in Fig. 8(a). The term subtracted from ^7K to obtain these results is shown by the solid line in Fig. 8(b). Note that the solid line in Fig. 8(b) lies slightly above the solid line in Fig. 6(b), since larger values of U were used for the underdoped $YBa_2Cu_3O_{6+x}$. These calculations are shown for four different values of V_1: $-0.125t$ (short-dashed), $-0.15t$ (solid), $-0.175t$ (long-dashed), and 0 (dot-dashed). These results have been obtained by using $U(T)$ represented by the solid curve in Fig. 2(b). Hence, they correspond to the first scenario described above where T_2^{-1} has been linearly extrapolated for $T < 160$ K. For each value of V_1, the calculations of δ^7K have been repeated according to the second scenario, where the saturation of T_2^{-1} below 160 K is attributed to the saturation of the antiferromagnetic correlations. In this case, the values of $U(T)$ shown by the dotted curve in Fig. 2(b) were used. In Fig. 8(a), these results are shown by the dotted curves for each value of V_1 as indicated. Comparing the results of the calculations with the experimental data, one sees that the values of V_1 between $-0.125t$ and $-0.15t$ would produce a fit of the experimental data on δ^7K.

Next, the results for ^{89}Y are discussed. The experiments by Mahajan et al. [1,4] found that Zn substitution in underdoped $YBa_2Cu_3O_{6+x}$ strongly modifies the nuclear resonance spectrum of ^{89}Y. In

this case, in addition to the main ^{89}Y resonance line, two satellite peaks are observed. These outer and middle resonance lines have been identified as belonging to the ^{89}Y nuclear spins which are respectively the first and the second near-neighbors of the Zn impurity, Y(1) and Y(2) in Fig. 5. The fact that the magnetic resonance spectrum of ^{89}Y in Li substituted $YBa_2Cu_3O_{6+x}$ is nearly the same as in Zn substituted samples confirms this identification [2]. In the following, the data on ^{89}K will be compared with the results of the calculations which were outlined in Section 3. However, the comparisons will not be carried out directly for ^{89}K. Rather, the shift of the satellite lines with respect to the main line will be used in order to compensate for the opening of the pseudogap in the pure system. Hence, the comparisons will be carried out for the following quantities,

$$\begin{aligned}\delta^{89}K\ (\text{outer}) &= {}^{89}K\ (\text{outer}) - {}^{89}K\ (\text{main})\\ \delta^{89}K\ (\text{middle}) &= {}^{89}K\ (\text{middle}) - {}^{89}K\ (\text{main}).\end{aligned} \tag{29}$$

Since ^{89}K (main) in Zn substituted material nearly follows the T dependence of ^{89}K in the pure system, $\delta^{89}K$ (outer) and $\delta^{89}K$ (middle) represent the change in the Knight shifts of the nuclear spins at the Y(1) and Y(2) sites, respectively, due to the substitution of the Zn impurity.

In Fig. 9(a) and (b), the points represent the experimental data on $-\delta^{89}K$ (outer) and $-\delta^{89}K$ (middle), respectively, for underdoped $YBa_2Cu_3O_{6+x}$ measured by Mahajan et al. [1,4]. In these figures, the data points are shown for two different orientations of the magnetic field **H**. It is estimated that the ^{89}Y hyperfine coupling has an anisotropy of about 15%, which could be the cause of the anisotropy of the data seen in Fig. 9(a) and (b) [4,40]. In Fig. 9(a), the error bars shown for the lowest and the highest temperature measurements are representative of the error bars for the other data points. In Fig. 9(b), the data points are shown up to 130 K, since at higher temperatures the middle satellite is not resolved.

The curves in Fig. 9(a) and (b) represent the results of the calculations for $-\delta^{89}K$ (outer) and $-\delta^{89}K$ (middle), respectively. These calculations have been carried out for the same values of V_1 as in Fig. 8(a) for δ^7K. [1] For $T < 160$ K, these calculations were carried out in two ways by using $U(T)$ shown by the solid and the dotted curves in Fig. 2(b). In Fig. 9(a) and (b), it is seen that for V_1 between $-0.125t$ and $-0.15t$, the data can be fitted. Finally, in Fig. 10 the T dependence of $^{63}K_c(\mathbf{r}_i)$ in underdoped $YBa_2Cu_3O_{6+x}$ is shown for various Cu(2) sites near the impurity. Here, $V_1 = -0.15t$ was used. In order to interpret these, in the next section the real-space structure of the changes induced in the magnetic correlations by the impurity will be shown. The $^{63}K_c$ measurements in Zn substituted $YBa_2Cu_3O_{6.7}$ imply that the polarization around the impurity is staggered [7].

3.3. Pattern of magnetic correlations around the impurity

In Fig. 11(a), $k(\mathbf{r})$ defined by Eq. (20), is shown as a function of the lattice distance $r = |\mathbf{r}|$ away from the impurity at $T = 100$ K. Here, r is given in units of the lattice constant, and in obtaining these results $V_1 = -0.15t$ was used. The horizontal long-dashed line denotes what is expected for $k(\mathbf{r})$ within this model for pure optimally doped $YBa_2Cu_3O_{6+x}$, and the open circles represent $k(\mathbf{r})$ when an impurity is introduced into this material at $\mathbf{r}_0 = 0$. The results for underdoped $YBa_2Cu_3O_{6+x}$ are also shown in Fig. 11(a). The dotted horizontal line denotes $k(\mathbf{r})$ for pure underdoped $YBa_2Cu_3O_{6+x}$, while the filled circles show $k(\mathbf{r})$ within the presence of the impurity for this material. The results on underdoped $YBa_2Cu_3O_{6+x}$ were obtained using the value of U given by the solid curve in Fig. 2(b). Note that, for underdoped $YBa_2Cu_3O_{6+x}$ in this graph, the physically more relevant quantity is the

[1] When the magnetic resonance spectrum of ^{89}Y in underdoped $YBa_2Cu_3O_{6+x}$ with Zn impurities is compared with the ^{89}Y spectrum within the presence of Li impurities, it is found that ^{89}K (outer) and ^{89}K (middle) are shifted by about 20% more to higher values for Li compared to Zn [2]. This could be because the stoichiometry of the Zn substituted and the Li substituted samples might be different [2]. For this reason, it would have been probably better to divide the calculated values of $\delta^{89}K$'s by a factor of 1.2 before comparing them with the $\delta^{89}K$ experimental data. However, this will not qualitatively affect the fits seen in Fig. 9(a) and (b).

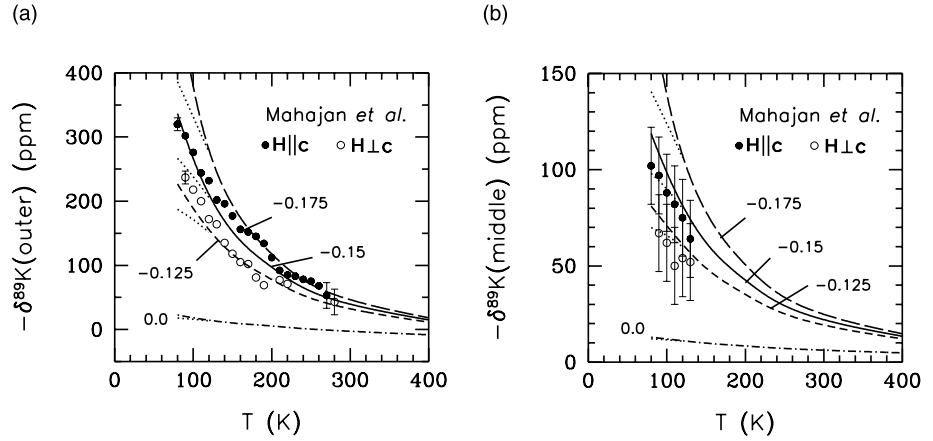

Fig. 9. (a) Temperature dependence of $-\delta^{89}K$ (outer) in underdoped $YBa_2Cu_3O_{6+x}$ with Zn impurities. Here, $\delta^{89}K$ (outer) is defined as the shift of the outer ^{89}Y satellite with respect to the ^{89}Y main resonance line. The open and the filled circles represent the experimental data on $-\delta^{89}K$ (outer) in underdoped $YBa_2Cu_3O_{6+x}$ with Zn impurities for the magnetic field $\mathbf{H}\|c$ and $\mathbf{H}\perp c$, respectively [1,4]. The curves represent the results obtained by using various values of V_1/t which are indicated next to the curves for the Y(1) site, which is the nearest ^{89}Y neighbor of the nonmagnetic impurity. (b) Results similar to those in (a) but for $-\delta^{89}K$ (middle). Here, $\delta^{89}K$ (middle) is defined as the shift of the middle ^{89}Y resonance line with respect to the main line. The curves represent results for various values of V_1/t for the Y(2) site, which is the second-nearest ^{89}Y neighbor of the nonmagnetic impurity.

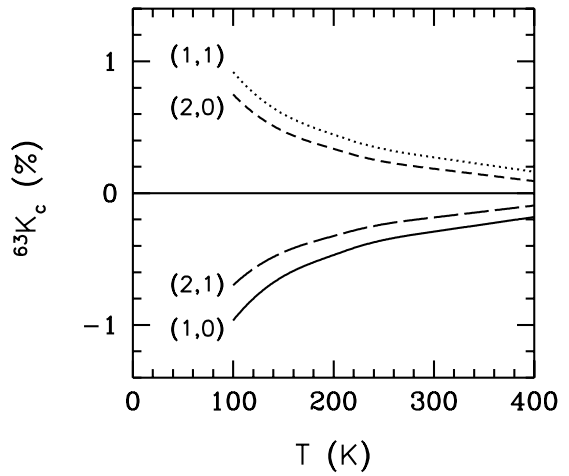

Fig. 10. Temperature dependence of the $^{63}Cu(2)$ Knight shift for $\mathbf{H}\|c$, $^{63}K_c(\mathbf{r}_i)$, in underdoped $YBa_2Cu_3O_{6+x}$ at sites $\mathbf{r}_i$ which are indicated next to the curves. These results were obtained for $V_1 = -0.15t$ using the values of $U(T)$ given by the solid curve in Fig. 2(b).

change in $k(\mathbf{r})$ induced by the impurity, since the presence of the pseudogap in the uniform susceptibility of the pure system is not included in the model.

The real-space structure of $k(\mathbf{r})$ is important since it determines the Knight shift at various sites. For instance, $k(\mathbf{r})$ at $\mathbf{r} = (1,0)$ determines the value of ^7K. On the other hand, $\delta^{89}K$ (outer), corresponding to the Y(1) site in Fig. 5, is given by the change in

$$k(0,0) + 2k(1,0) + k(1,1) \tag{30}$$

induced by the impurity. Similarly, $\delta^{89}K$ (middle), corresponding to the Y(2) site, probes the change induced in

$$k(1,0) + k(1,1) + k(2,0) + k(2,1) \tag{31}$$

by the impurity. Hence, it is seen that by the fitting of δ^7K in Fig. 8(a), the value of $k(1,0)$ is fixed. Since it is known that $k(0,0)$ vanishes when the impurity is introduced, the fitting of $\delta^{89}K$ (outer) in Fig. 9(a) fixes the value of $k(1,1)$. In Fig. 11(a), it is seen that while $k(1,0)$ is enhanced strongly by the impurity, $k(1,1)$ is strongly suppressed and it even becomes negative. The fact that both δ^7K and $\delta^{89}K$ (outer) can be fitted at the same time means that the induced changes in $k(\mathbf{r})$ of the actual system must have a staggered pattern at the sites $(1,0)$ and $(1,1)$. Since $k(1,0)$ and $k(1,1)$ are now fixed, the fact that $\delta^{89}K$ (middle) can also be fitted

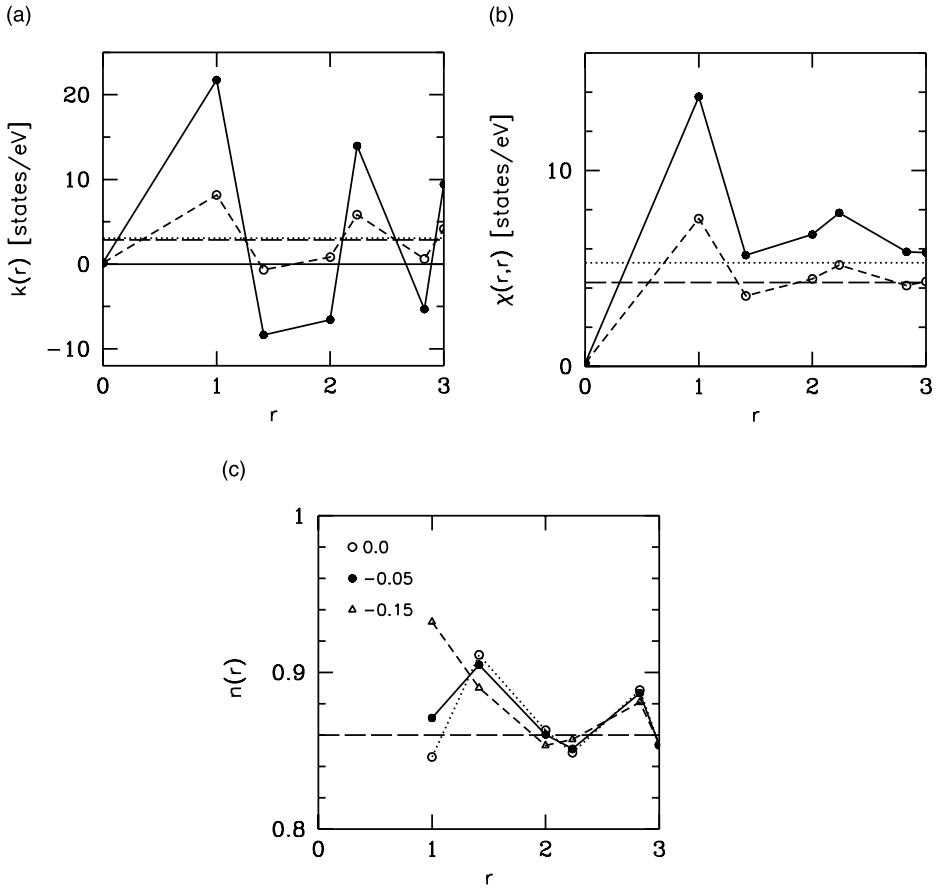

Fig. 11. (a) $k(\mathbf{r})$ versus the distance r away from the impurity in units of the lattice spacing a for $T = 100$ K and $V_1 = -0.15t$. Here, the open and the filled circles represent the results for the optimally doped and the underdoped $YBa_2Cu_3O_{6+x}$, respectively. Also, the horizontal long-dashed and dotted lines represent $k(\mathbf{r})$ for the optimally doped and underdoped pure systems, respectively. (b) $\chi(\mathbf{r},\mathbf{r})$ versus the distance r away from the impurity presented in the same way as in (a) for $k(\mathbf{r})$. (c) Electron occupation $n(\mathbf{r}_i)$ at sites $\mathbf{r}_i$ near the impurity plotted as a function $r = |\mathbf{r}_i|$ at 100 K. These results were obtained for $V_1/t = -0.15$ with $W = 1$ eV (—) and for $V_1/t = -0.05$ with $W = 3$ eV (- - -). Also shown are results for an onsite impurity potential ($V_1 = 0$) and $W = 1$ eV ($\cdots$). In all of these cases, $V_0 = -100t$ was used.

means that the change in $k(2,0) + k(2,1)$ is fixed. In Fig. 11(a), it is seen that $k(2,0)$ gets suppressed by the impurity and $k(2,1)$ gets enhanced while the total effect on $k(2,0) + k(2,1)$ is small. This in turn means that the induced changes in $k(\mathbf{r})$ of the actual system must also be staggered at sites $(2,0)$ and $(2,1)$. Hence, the fits obtained in Figs. 8(a), 9(a) and (b) imply that $k(\mathbf{r})$ has a staggered pattern in the vicinity of the impurity. This conclusion was reached by the analysis of Mahajan et al. [1,4]. Here it is seen that this simple model produces this pattern as well.

It is useful to compare the staggered pattern of $k(\mathbf{r})$ with the pattern of $\chi(\mathbf{r},\mathbf{r})$ near the impurity. Fig. 11(b) shows $\chi(\mathbf{r},\mathbf{r})$ versus r plotted in the same way as $k(\mathbf{r})$ is plotted in Fig. 11(a). Here one sees that $\chi(\mathbf{r},\mathbf{r})$ is strongly modified near the impurity. It is also seen that $\chi(\mathbf{r},\mathbf{r})$ does not have a staggered pattern as, for instance, one would have had for antiferromagnetically ordered spins. The comparisons shown in Figs. 6, 8 and 9 mean that the experimental data on ^7K and ^{89}K require a staggered pattern for $k(\mathbf{r})$ in the vicinity of the impurity. But a staggered structure for $\chi(\mathbf{r},\mathbf{r})$ is not necessary.

In Fig. 11(a) and (b), it is seen that while $\chi(\mathbf{r},\mathbf{r})$ is positive for all $\mathbf{r}$, $k(\mathbf{r})$ can become negative, for instance at $\mathbf{r}=(1,1)$. This is possible because $\chi(\mathbf{r},\mathbf{r}')$ for $\mathbf{r}=(1,0)$ and $\mathbf{r}'=(1,1)$ has a large negative value after the impurity is introduced, meaning that the impurity is inducing strong antiferromagnetic correlations in its local environment in this model. These points will be discussed further in Section 4.1.

At this point it is also useful to present results on how the impurity potential affects the single-particle properties. For this purpose, in Fig. 11(c) the electron occupation number $n(\mathbf{r}_i)=\sum_\sigma\langle c^\dagger_{i\sigma}c_{i\sigma}\rangle$ for sites near the impurity is shown as a function of the distance $r=|\mathbf{r}_i|$ from the impurity for various values of V_1/t. Since V_0 is strongly attractive, the impurity site which is not shown in this figure, is nearly doubly occupied, $n(\mathbf{r}_i=0)\approx 2.0$. For $V_1=0$, it is seen that $n(\mathbf{r}_i)$ is enhanced at $\mathbf{r}_i=(1,1)$ with respect to its value at $\mathbf{r}_i=(1,0)$. Away from the impurity, these oscillation in $n(\mathbf{r}_i)$ decay, and $n(\mathbf{r}_i)$ goes to its value in the pure system, $\langle n\rangle=0.86$, which is indicated by the horizontal long-dashed line. Here, it is also seen that this structure in $n(\mathbf{r}_i)$ holds for weak attractive values of V_1. But as V_1 becomes more attractive, for instance for $V_1=-0.15t$, the pattern in $n(\mathbf{r}_i)$ changes. In this case, $n(\mathbf{r}_i=(1,0))$ gets enhanced over $n(\mathbf{r}_i=(1,1))$. Hence, in Fig. 11(c) one observes that the structure in $n(\mathbf{r}_i)$ in the vicinity of the impurity does not necessarily reflect the sign of V_1. For instance, a finite attractive V_1 is required before $n(\mathbf{r}_i=(1,0))$ gets enhanced with respect to $n(\mathbf{r}_i=(1,1))$. This has to do with the presence of the strongly attractive V_0 term in the impurity potential.

In Section 3.2, it was seen that the data on δ^7K and $\delta^{89}K$ can be fitted reasonably well over the whole temperature range by using a simple form for the effective impurity potential without any T dependence. On the other hand, because of the various approximations employed in this model, the quantitative agreement obtained in the fits might actually be misleading. However, what is significant is the fact that δ^7K, $\delta^{89}K$ (outer) and $\delta^{89}K$ (middle) can be fitted all at the same time, which means that the real-space structure of the changes induced in the magnetic correlations near the impurity appears to be described by this simple model.

4. Discussion

4.1. Role of antiferromagnetic correlations

It is useful to discuss the connection between the antiferromagnetic correlations of the system which is composed of the impurity and the host, and the anomalous enhancement of the Knight shift at sites around the impurity. This connection becomes more clear if the Fourier transform $\chi(\mathbf{q},\mathbf{q}')$ is introduced,

$$\chi(\mathbf{q},\mathbf{q}')=\sum_{\mathbf{r},\mathbf{r}'} e^{i(\mathbf{q}\cdot\mathbf{r}-\mathbf{q}'\cdot\mathbf{r}')}\chi(\mathbf{r},\mathbf{r}'). \tag{32}$$

Note that $\chi(\mathbf{r},\mathbf{r}')$ is the susceptibility for an N-site square lattice with one impurity at the center and periodic boundary conditions.

An especially important quantity is the off-diagonal susceptibility $\chi(\mathbf{q},0)\equiv\chi(\mathbf{q},\mathbf{q}'=0)$, since its Fourier transform with respect to $\mathbf{q}$ gives $k(\mathbf{r})$. Particularly, at sites $\mathbf{r}=(1,0)$ and $(1,1)$ with respect to the impurity, one has

$$\begin{aligned} k(1,0)&=\sum_{\mathbf{q}}\tfrac{1}{2}(\cos q_x+\cos q_y)\chi(\mathbf{q},0)\\ k(1,1)&=\sum_{\mathbf{q}}\cos(q_x+q_y)\chi(\mathbf{q},0). \end{aligned} \tag{33}$$

In Fig. 12(a) and (b), the $\mathbf{q}$ dependence of $-\chi_0(\mathbf{q},0)$, which is for $U=0$, and $-\chi(\mathbf{q},0)$ are shown at 100 K for optimally doped $YBa_2Cu_3O_{6+x}$ obtained by using $V_1=-0.15t$. [2] Here, the δ-function component of $\chi(\mathbf{q},\mathbf{q}'=0)$ at $\mathbf{q}=0$ has been omitted. In these figures, it is seen that $-\chi(\mathbf{q},0)$ is enhanced with respect to $-\chi_0(\mathbf{q},0)$, and they both peak at $\mathbf{q}$ near (π,π). Note that for $\mathbf{q}\sim(\pi,\pi)$, the form factors entering Eq. (33), $\frac{1}{2}(\cos q_x+\cos q_y)\sim -1$ and $\cos(q_x+q_y)\sim 1$.

[2] $\chi(\mathbf{q},\mathbf{q}'=0)$ seen in Fig. 12(b) is not a smooth curve, hence one could expect large finite size effects on the Knight shifts. This is not the case because of the way the calculation of $\chi(\mathbf{r},\mathbf{r}')$ is carried out. As described in Ref. [21], $\chi_0(\mathbf{r},\mathbf{r}')$ is calculated on a small lattice (28×28), however by using $G_0(\mathbf{r}_i,\mathbf{r}_j,i\omega_n)$ and $\chi_0^{\mathrm{L}}(\mathbf{q})$ calculated on large lattices. Hence, when the RPA equation is solved for $\chi(\mathbf{r},\mathbf{r}')$ on the small lattice, the local quantities such as the Knight shifts for the sites near the impurity have small finite size effects, even though $\chi(\mathbf{q},\mathbf{q}'=0)$ obtained from $\chi(\mathbf{r},\mathbf{r}')$ is not a smooth curve.

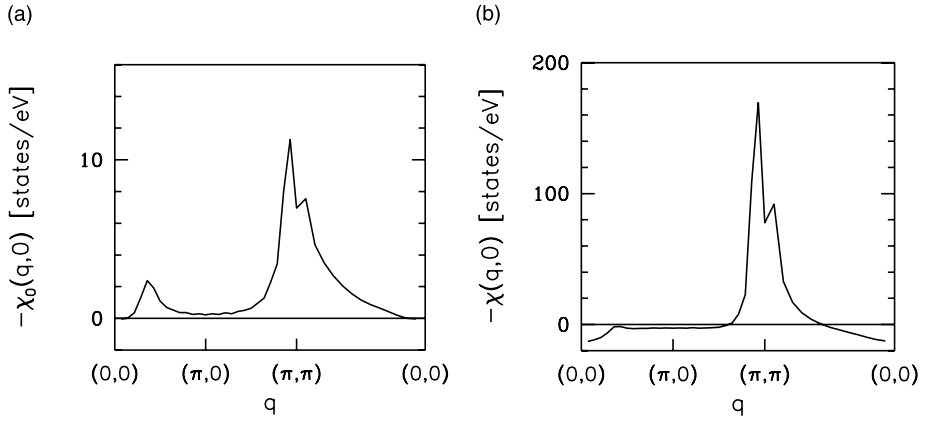

Fig. 12. Off-diagonal susceptibilities (a) $-\chi_0(\mathbf{q},\mathbf{q}'=0)$ and (b) $-\chi(\mathbf{q},\mathbf{q}'=0)$ versus $\mathbf{q}$ obtained by using $V_1=-0.15t$ for optimally doped $YBa_2Cu_3O_{6+x}$ at $T=100$ K. Here, the δ-function components at $\mathbf{q}=\mathbf{q}'=0$ have been omitted.

Because of the $\mathbf{q}$ structure of $\chi(\mathbf{q},0)$, $k(1,0)$ gets enhanced and $k(1,1)$ gets suppressed. Hence, within this model, the staggered pattern of $k(\mathbf{r})$ near the impurity is a consequence of the peaking of $-\chi(\mathbf{q},0)$ near (π,π).

The enhancement of $-\chi(\mathbf{q},0)$ with respect to $-\chi_0(\mathbf{q},0)$ is understood better if the RPA equation, (17), is written in momentum space,

$$\chi(\mathbf{q},\mathbf{q}')=\chi_0(\mathbf{q},\mathbf{q}')+U\sum_{\mathbf{q}''}\chi_0(\mathbf{q},\mathbf{q}'')\chi(\mathbf{q}'',\mathbf{q}'), \quad (34)$$

where $\chi_0(\mathbf{q},\mathbf{q}')$ is for $U=0$. For the pure system, $\chi(\mathbf{q},\mathbf{q}'=0)$ is given by

$$\chi(\mathbf{q},0)=N\delta_{\mathbf{q},0}\chi_{\text{pure}}(\mathbf{q}\to 0), \quad (35)$$

where χ_{pure} is defined by Eq. (4), and within the presence of the impurity $\chi(\mathbf{q},\mathbf{q}'=0)$ is obtained by solving

$$\chi(\mathbf{q},0)=\chi_0(\mathbf{q},0)+U\sum_{\mathbf{q}''}\chi_0(\mathbf{q}'',0)\chi(\mathbf{q}'',\mathbf{q}). \quad (36)$$

This expression shows that when $\mathbf{q}''\sim(\pi,\pi)$, $\chi(\mathbf{q}\sim(\pi,\pi),\mathbf{q}'=0)$ couples to the antiferromagnetic correlations determined by $\chi(\mathbf{q},\mathbf{q})$ with $\mathbf{q}\sim(\pi,\pi)$ of the system which is composed of the host and the impurity. This is the reason for the strong enhancement of $\chi(\mathbf{q},\mathbf{q}'=0)$ with respect to $\chi_0(\mathbf{q},\mathbf{q}'=0)$.

It is useful to discuss the physical meaning of the off-diagonal susceptibility $\chi_0(\mathbf{q},\mathbf{q}')$ where $\mathbf{q}\neq\mathbf{q}'$. During the scattering of the spin fluctuations by the impurity potential, the momentum is not conserved and $\chi_0(\mathbf{q},\mathbf{q}\neq\mathbf{q}')$ acts as the vertex for the scattering of the spin fluctuations by the impurity with $\mathbf{Q}^*=\mathbf{q}-\mathbf{q}'$ momentum transfers. The peaking of $\chi_0(\mathbf{q},\mathbf{q}'=0)$ near $\mathbf{q}\sim(\pi,\pi)$ means that the scattering of the antiferromagnetic spin fluctuations with momentum transfers near (π,π) is the dominant scattering process. The effects of the scatterings with large momentum transfers on the $\mathbf{Q}=(\pi,\pi)$ neutron scattering intensity have been also emphasized in Ref. [22], where $\chi_0(\mathbf{q},\mathbf{q}')$ was calculated at the lowest order in the impurity potential. Within this model, both the Knight shifts and the neutron scattering experiments point out at the importance of the scattering of the particle–hole pairs by the nonmagnetic impurity with large momentum transfers near $2\mathbf{k}_F$. If the $\sim 2\mathbf{k}_F$ scatterings are indeed one of the primary effects of the nonmagnetic impurities, then an anomalous softening of the phonons at wave vectors $\sim 2\mathbf{k}_F$ might be observed in $YBa_2Cu_3O_{6+x}$ with dilute Zn impurities [43].

The real-space pattern of $^{63}K_c(\mathbf{r}_i)$ seen in Fig. 7(b) also reflects the $\mathbf{q}$ dependence of $\chi(\mathbf{q},\mathbf{q}'=0)$. Eq. (26) for $^{63}K_c(\mathbf{r}_i)$ can be rewritten as

$$^{63}K_c(\mathbf{r}_i)=\frac{1}{2}\left(\frac{\gamma_e}{^{63}\gamma_n}\right)\frac{1}{N}\sum_{\mathbf{q}}e^{i\mathbf{q}\cdot\mathbf{r}_i}\left(A_c+4B\gamma_{\mathbf{q}}\right)\chi(\mathbf{q},0), \quad (37)$$

where $\gamma_{\mathbf{q}} = (\cos q_x + \cos q_y)/2$. Since $\chi(\mathbf{q}, \mathbf{q}' = 0)$ has most of its weight at $\mathbf{q} \sim (\pi, \pi)$ for which $\gamma_{\mathbf{q}} \sim -1$, one gets

$$^{63}K_c(\mathbf{r}_i) \approx -\frac{1}{2}(|A_c| + 4B)\left(\frac{\gamma_e}{^{63}\gamma_n}\right)\frac{1}{N}\sum_{\mathbf{q}\sim(\pi,\pi)} e^{i\mathbf{q}\cdot\mathbf{r}_i}\chi(\mathbf{q}, 0). \tag{38}$$

Here one sees that $|A_c| + 4B$ has a large value and $^{63}K_c(\mathbf{r}_i)$ directly couples to $\chi(\mathbf{q} \sim (\pi, \pi), \mathbf{q}' = 0)$. It has been noted in Ref. [7] that the anomalous broadening of the ^{63}Cu(2) linewidth reflects the staggered polarization of the magnetic correlations near the impurity. It is important to note that, within this model, the antiferromagnetic correlations also get enhanced due to the presence of the impurity [21]. If N_i randomly distributed nonmagnetic impurities are considered in the dilute limit, then the **q**-dependent magnetic susceptibility of this system is given by

$$\chi(\mathbf{q}) \equiv \chi_{\text{pure}}(\mathbf{q}) + n_i N\big[\chi(\mathbf{q}, \mathbf{q}) - \chi_{\text{pure}}(\mathbf{q})\big], \tag{39}$$

where $n_i = N_i/N$ is the impurity concentration. The results on $\chi(\mathbf{Q}^*)$ for 0.5% nonmagnetic impurities are compared with $\chi_{\text{pure}}(\mathbf{Q}^*)$ in Fig. 3(b) and (c), where it is seen that the impure system has stronger antiferromagnetic correlations than the pure system. Here, $\mathbf{Q}^*$ is the incommensurate wave vector where χ peaks at low temperatures. The enhancement of $\chi(\mathbf{Q}^*)$ over $\chi_{\text{pure}}(\mathbf{Q}^*)$ is especially significant for the underdoped system. Hence, it needs to be noted that the enhancement of the Knight shifts near the impurity in this model is a result of the coupling to $\chi(\mathbf{q}, \mathbf{q})$ for $\mathbf{q} \sim (\pi, \pi)$ of the whole system which is composed of the impurity and the host rather than to $\chi_{\text{pure}}(\mathbf{q} \sim (\pi, \pi))$ of the pure host.

Experimentally, $\text{Im}\,\chi(\mathbf{Q}, \omega)$ is the inelastic neutron scattering spectral weight. The enhancement of $\text{Im}\,\chi(\mathbf{Q}, \omega)$ in the normal state by the impurity scattering is clearly seen for dilute Zn impurities in $YBa_2Cu_3O_7$ [12–14]. The low frequency part of $\text{Im}\,\chi$ is also probed by the measurement of the longitudinal relaxation rate T_1^{-1} at sites near the impurity. The measurements of T_1^{-1} at sites near the impurity have found interesting results [1,4, 6,7]. The calculations presented here have been extended to obtain the ^{7}Li T_1^{-1} using the Pade approximation for analytic continuation to the real-frequency axis of the results calculated in terms of the Matsubara frequencies. While it is difficult to obtain reliable results on $\text{Im}\,\chi(\mathbf{Q}, \omega)$ for general ω using the Pade approximation, it is possible to obtain control on the calculation of T_1^{-1}, which requires only the $\omega \to 0$ limit. Since the analytic continuation procedure requires special attention, the calculations of the ^{7}Li T_1^{-1} will be presented elsewhere [41]. [3]

4.2. Effects of the pseudogap in underdoped $YBa_2Cu_3O_{6+x}$

The analysis carried out for underdoped $YBa_2Cu_3O_{6+x}$ needs to be interpreted carefully because of the presence of the pseudogap in this system. The uniform susceptibility of pure $YBa_2Cu_3O_{6.63}$ starts to decrease below 300 K, with a T dependence proportional to that given by the dashed curve in Fig. 8(b). This has been ignored in the calculations presented above. In order to explore the effects of the pseudogap on the Knight shift results, the following simple calculation has been carried out. The suppression of the diagonal irreducible susceptibility $\chi_0(\mathbf{q}, \mathbf{q})$ for $\mathbf{q} \sim 0$ has been artificially incorporated into the model by multiplying $\chi_0(\mathbf{q}, \mathbf{q})$ by the factor

$$F(\mathbf{q}) = 1 - a\,e^{-|\mathbf{q}|^2/\kappa^2}, \tag{40}$$

which has been chosen in order to cause a suppression for $\mathbf{q} \sim 0$. After artificially suppressing the diagonal irreducible susceptibility for $\mathbf{q} \sim 0$, the Fourier transform is taken to obtain $\chi_0(\mathbf{r}, \mathbf{r}')$ of the pure system, which is then used in calculating $\chi_0(\mathbf{r}, \mathbf{r}')$ of the impure system. Hence, in this procedure, the diagonal terms $\chi_0(\mathbf{q}, \mathbf{q})$ for $\mathbf{q} \sim 0$ of the impure system have the effects of the pseudogap, but $\chi_0(\mathbf{q}, \mathbf{q})$ for $\mathbf{q} \sim (\pi, \pi)$ and the off-diagonal terms $\chi_0(\mathbf{q}, \mathbf{q}')$, where $\mathbf{q} \neq \mathbf{q}'$, are not affected by this artificial opening of the pseudogap. Next, $\chi_0(\mathbf{r}, \mathbf{r}')$ calculated with this procedure was used in

[3] Comparisons with the ^{7}Li T_1^{-1} data will also be useful in estimating the magnitude of the ^{7}Li hyperfine coupling.

solving Eq. (17) for $\chi(\mathbf{r},\mathbf{r}')$ and in determining the Knight shifts. The parameter κ entering Eq. (40) was arbitrarily chosen to be $\pi/2$. In addition, a has been chosen such that the ratio of

$$\frac{F(0)\chi_0^{\mathrm{L}}(0)}{1-UF(0)\chi_0^{\mathrm{L}}(0)} \tag{41}$$

to $\chi_0^{\mathrm{L}}(0)/(1-U\chi_0^{\mathrm{L}}(0))$ is equal to the ratio of ^{89}K in pure underdoped $YBa_2Cu_3O_{6+x}$ to that in pure optimally doped $YBa_2Cu_3O_{6+x}$. For instance, at $T=100$ K, this condition is satisfied by using $a=0.51$. The opening of the pseudogap in this way requires slightly larger values of V_1 for fitting the Knight shift data. In Section 3.2, the data on δ^7K, $\delta^{89}K$ (outer) and $\delta^{89}K$ (middle) were fitted by using V_1 between $-0.125t$ and $-0.15t$. Here, if $V_1=-0.15t$ is used along with the above mentioned values of κ and a, then at $T=100$ K one obtains the following results for the Knight shifts: $\delta^7K=650$ ppm, $\delta^{89}K$ (outer) $=-180$ ppm, and $\delta^{89}K$ (middle) $=-75$ ppm. On the other hand, at 300 K, it is necessary to use $a=0.25$ and in this case one obtains: $\delta^7K=250$ ppm, $\delta^{89}K$ (outer) $=-35$ ppm, and $\delta^{89}K$ (middle) $=-20$ ppm. These values for the Knight shifts are comparable to the data seen in Figs. 8(a) and 9. Hence, when the pseudogap is introduced in $\chi_0(\mathbf{q},\mathbf{q})$ for $\mathbf{q}\sim 0$ in this artificial way, the Knight shift data can be still fitted, but by using a slightly larger value for V_1. However, it must be kept in mind that the way the pseudogap is introduced here is not rigorous, and in fact the fitting of the data in this way can be considered as superfluous. For this reason, the fitting of the data on the underdoped compound will not be pursued further. Rather, here it is only pointed out that the staggered nature of the induced magnetic correlations seen in this model appears to be consistent with the measurements of the ^{7}Li and ^{89}Y Knight shifts in underdoped $YBa_2Cu_3O_{6+x}$.

4.3. Dependence of the results on the effective bandwidth

The results seen in Section 3 were obtained by using an effective bandwidth W of 1 eV. For a one-band model of the cuprates, the bare hopping matrix element is estimated to be of order 0.45 eV leading to a bare bandwidth of 3.6 eV. While in principle one expects that the Coulomb correlations act to reduce the bandwidth, it is not clear what the precise value of the effective bandwidth should be in an RPA framework. Hence, it is necessary to check the dependence of the results on the effective bandwidth W, which was assumed to be 1 eV in Section 3. For this reason, here, the Knight shifts are calculated for $W=3$ eV. In this case, larger values of U are required for fitting the T_2^{-1} data and, consequently, the pure system has a stronger Stoner enhancement of the antiferromagnetic correlations. For $W=3$ eV, the value of the ^{89}Y hyperfine coupling D was chosen to be -2 kOe/μ_{B} in order to fit the value of ^{89}K for pure $YBa_2Cu_3O_7$ in the normal state. The experimental estimate for D is also about -2 kOe/μ_{B} [4].

In Fig. 13, ^7K versus T is shown for optimally doped $YBa_2Cu_3O_{6+x}$ calculated using $W=3$ eV.

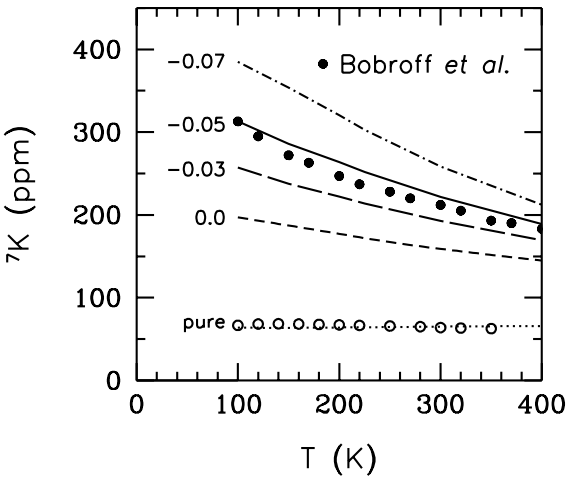

Fig. 13. Temperature dependence of ^7K for optimally doped $YBa_2Cu_3O_{6+x}$, obtained for various values of V_1/t. These results are for an effective bandwidth of 3 eV, and here the ^{7}Li hyperfine coupling C was taken to be 1.4 kOe/μ_{B}. The filled circles represent the ^7K data on optimally doped $YBa_2Cu_3O_{6+x}$ by Bobroff et al. [2]. The open circles represent the estimate of $^7K_0$ obtained by using the ^{89}K data [39] on pure optimally doped $YBa_2Cu_3O_{6+x}$. Here, the ^{89}Y hyperfine coupling was taken to be -2 kOe/μ_{B}. The dotted curve has been obtained by using $V_0=V_1=0$ and the remaining curves have been obtained by using $V_0=-100t$ and the values of V_1/t which are indicated next to the curves.

Here, the ^{7}Li hyperfine coupling C was taken to be 1.4 kOe/μ_B. The open circles represent $^7K_0$ deduced from the ^{89}K data [39] on pure $YBa_2Cu_3O_7$. The dotted curve represents the theoretical results for $^7K_0$. Here, it is seen that a smaller value of V_1 is required for fitting the ^7K data as compared to that for $W = 1$ eV. This is because in this case the antiferromagnetic correlations are stronger.

It is also necessary to compare the value of C used here with the experimental estimate. In Ref. [2], C was estimated to be 2.4 kOe/μ_B. This value was deduced by comparing the enhancement of the uniform susceptibility $\Delta\chi$ with the enhancement of ^7K for the underdoped $YBa_2Cu_3O_{6+x}$ by assuming that the contribution to $\Delta\chi$ is arising from the changes in the magnetic correlations at only the four nearest-neighbor Cu(2) sites of the impurity. Note, however, that $\Delta\chi$ is given by

$$\Delta\chi = \sum_j k(\mathbf{r}_j) - \chi_{\text{pure}}(\mathbf{q} \to 0), \tag{42}$$

where the sum over j is carried over the whole lattice, and the Knight shift data and the numerical results presented in this paper indicate that the changes induced in $k(\mathbf{r}_j)$ by the impurity is extended and not restricted to the four nearest-neighbor sites of the impurity. In fact, by limiting the changes in $k(\mathbf{r}_j)$ to be only at the nearest-neighbor sites, one would overestimate $\Delta\chi$. Similarly, when one calculates C by using the experimental data on $\Delta\chi$ and the ^7K data, one would overestimate C. For instance, in Fig. 11(a), it is seen that at 100 K the enhancement of $k(1,0)$ by the impurity, $\Delta k(1,0)$, is about 20 states/eV for underdoped $YBa_2Cu_3O_{6+x}$. If $\Delta\chi$ is estimated by just using the change in $k(1,0)$, then one would obtain $\Delta\chi = 0.4$ states/eV in the dilute limit for an impurity concentration of 0.5%. On the other hand, the calculated value of $\Delta\chi$ at $T = 100$ K and $V_1 = -0.15t$ for underdoped $YBa_2Cu_3O_{6+x}$ in this model is $\sim$0.2 states/eV. Hence, by using $\Delta k(1,0)$ and assuming that the changes in $k(\mathbf{r})$ occur only at the nearest-neighbor sites of the impurity, one would overestimate $\Delta\chi$ by about a factor of two. Similarly, if $\Delta k(1,0)$ and $\Delta\chi$ are used to calculate C one would overestimate C by the same amount. When this is taken into account, it is seen that the values of C used here, 0.85 kOe/μ_B in Section 3 and 1.4 kOe/μ_B in Section 4.3, are comparable to the experimental estimate which was obtained by using the data on $\Delta\chi$ and ^7K.

In Fig. 14(a)–(c), the T dependence of δ^7K, $-\delta^{89}K$(outer), and $-\delta^{89}K$(middle) are shown for underdoped $YBa_2Cu_3O_{6+x}$. Here, it is seen that for $V_1 = -0.03t$, the magnitudes of the calculated Knight shifts agree with the experimental data. However, the fitting of the T dependence of the Knight shifts is not as good as that seen in Section 3 for $W = 1$ eV.

The results presented in this section show that the value of V_1 required for fitting the Knight shift data depends on the effective bandwidth. For $W = 3$ eV, the system has stronger enhancement of the AF correlations compared to that for $W = 1$ eV. Here, it has been shown that as W increases V_1 required for fitting the data decreases. However, even if a W of 4 eV is used, at the level of RPA, an impurity potential with $V_1 = 0$ does not produce sufficient T variation for fitting the ^7K data on optimally doped $YBa_2Cu_3O_{6+x}$, and a weakly attractive V_1 is necessary.

4.4. Nature of the effective impurity potential

Because of the Coulomb correlations, the bare impurity potential which has only an onsite component $V_0 \sum_\sigma c^\dagger_{0\sigma} c_{0\sigma}$ could acquire an extended component through higher-order scattering processes [28]. How this could happen at lowest order in the Coulomb repulsion U is discussed in Appendix B. This extended component is modeled here by using a static V_1 as a free parameter. In this picture, the fact that the Knight shift data imply $V_1 < 0$ is giving information on the effective particle–particle interaction in the system. The real-space structure of the effective impurity interaction was studied at half-filling for the t–J model within the exact diagonalization calculations [28]. It is useful to calculate V_1 in exact numerical calculations away from half-filling. This would be a test of the model presented here. Furthermore, note that here V_1 is assumed to have no temperature dependence. However, V_1 could depend on T, if indeed the Coulomb correlations play a role in inducing the extended component of the impurity

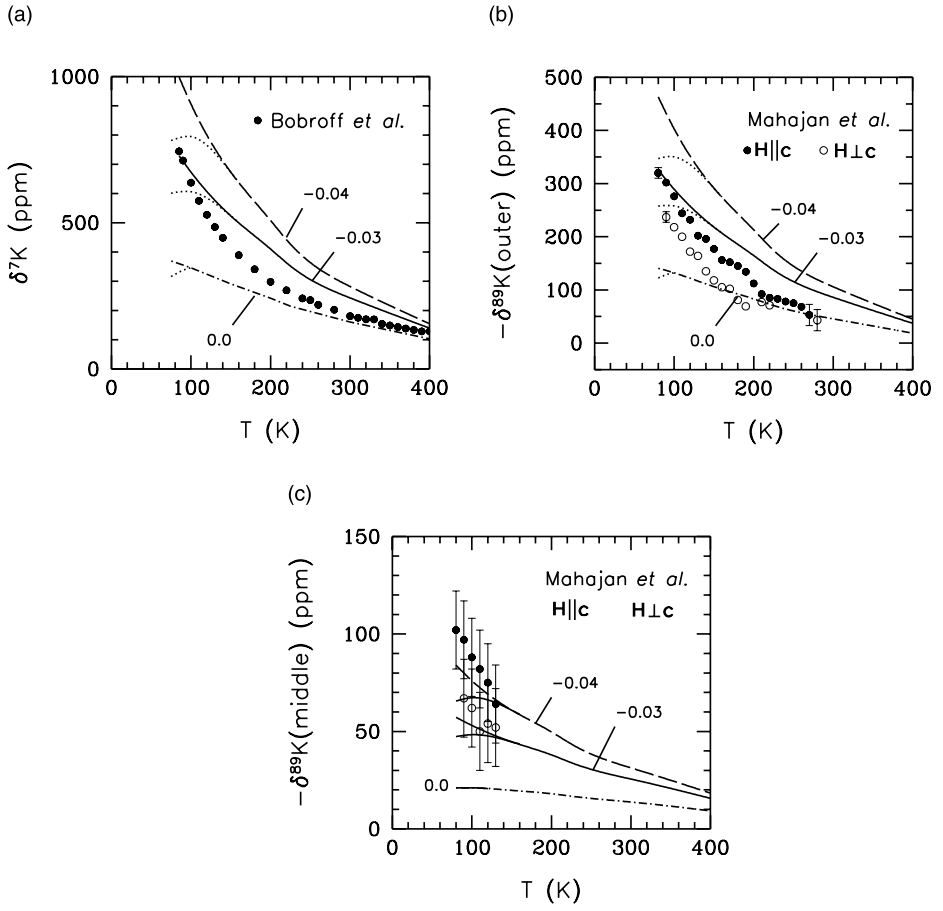

Fig. 14. Temperature dependence of (a) δ^7K, (b) $-\delta^{89}K$(outer) and (c) $-\delta^{89}K$(middle) for underdoped $YBa_2Cu_3O_{6+x}$ obtained by using various values of V_1/t which are indicated next to the curves. These results have been calculated by using an effective bandwidth W of 3 eV, as compared to $W = 1$ eV used in Figs. 8 and 9. In addition, here the ^{7}Li and the ^{89}Y hyperfine couplings were taken to be 1.4 kOe/μ_B and -2 kOe/μ_B, respectively. The experimental data in (a) are from Ref. [2], and the data in (b) and (c) are from Refs. [1,4].

potential. This could quantitatively affect the fits seen above.

These results carried out at the level of RPA imply that V_1 is weakly attractive. At this level, even though an onsite scattering potential ($V_1 = 0$) yields large enhancements of the Knight shifts, it is still insufficient for fitting the T dependence, for instance, of ^7K in optimally doped $YBa_2Cu_3O_{6+x}$. However, note that corrections beyond RPA might change this result. For instance, the spin-fluctuation self-energy corrections to the single-particle Green's functions, when taken into account self-consistently, could play an important role.

Within this model, the Knight shift experiments on the cuprates with nonmagnetic impurities are interesting especially because they probe the interplay of the correlations in the density and the magnetic channels. The effective impurity potential acts in the density channel while its spatially resolved magnetic response is detected through the Knight shift measurements. Similarly, the recent ^{7}Li Knight shift measurements [44] in the d-wave superconducting state of $YBa_2Cu_3O_{6+x}$ give valuable information about the interplay of the density, magnetic and the d-wave superconducting correlations in this material.

Another set of experiments which produce spatially resolved information on the effects of the nonmagnetic impurities are the STM measurements on Zn substituted BISCO [42]. These measurements have been carried out in the superconducting state. Clearly, similar STM measurements above T_c would be useful for understanding the effects of the nonmagnetic impurities in the normal state. This would allow for a direct comparison of the single-particle properties with this model.

It is also desirable to extend these model calculations to the superconducting state in order to make comparisons with the STM [42] and the recent NMR [44] measurements below T_c. However, note that if a spin-fluctuation mediated mechanism is assumed for the d-wave pairing, then the effects of the impurity on the pairing potential need to be taken into account as well as the scattering of the quasiparticles by the impurity. This is because it is already known in the normal state that in the local environment of the impurity the spin fluctuations are strongly modified [1–10].

Here, the effects of the scatterings by a nonmagnetic impurity on the magnetic spectrum is studied by modeling the impurity as a potential scatterer. In this respect, disorder could have effects similar to those of nonmagnetic impurities, and it has been already pointed out that the anomalous line broadening of $^{63}Cu(2)$ in $La_{2-x}Sr_xCuO_4$ could be due to the intrinsic disorder in this compound [45].

5. Summary and conclusions

In this paper, the Knight shift data on $YBa_2Cu_3O_{6+x}$ with nonmagnetic impurities have been analyzed within a rather simple model exhibiting short-range antiferromagnetic correlations. The antiferromagnetic correlations have been modeled within the framework of the 2D Hubbard model, and the effects of an impurity have been approximated by using a static extended impurity potential. The strength of the antiferromagnetic correlations in the pure system has been determined by fitting the T_2^{-1} data of pure $YBa_2Cu_3O_{6+x}$. The impurity potential has been assumed to have a range of just one lattice spacing without any temperature dependence. The onsite component of the impurity potential was taken to be strongly attractive, and the near-neighbor component V_1 was treated as a free parameter in fitting the Knight shift data. The simplicity of the model and the differences in the stoichiometry of the samples along with the uncertainities in the hyperfine couplings are factors which limit the conclusions which can be drawn. Nevertheless, here, it has been found that the anomalous T dependence of ^7K in $YBa_2Cu_3O_7$ can be fitted, if a weakly attractive V_1 is used. The nature of the effective impurity potential could be studied in the paramagnetic state of the Hubbard model, where there are short-range antiferromagnetic correlations, by using exact numerical methods. This could be a test of one of the main assumptions of this model. Especially, the sign of V_1 could be tested. These calculations have been also extended to the case of underdoped $YBa_2Cu_3O_{6+x}$ after making various assumptions about the magnetic correlations in this compound, which has a magnetic pseudogap. Based on these assumptions, it has been found that the real-space structure of the magnetic correlations in the vicinity of the impurity is consistent with the Knight shift experiments. However, caution is necessary in interpreting the results on underdoped $YBa_2Cu_3O_{6+x}$.

The results presented in this paper depend on the nature of the effective impurity potential used. Any magnetic scattering component in V_{eff} could significantly change the results. Furthermore, it needs to be kept in mind that the validity of these results depends on the weak-coupling approach used for calculating the magnetic correlations. Clearly, much remains to be understood about the effects of the Zn or Li impurities on the magnetic correlations of $YBa_2Cu_3O_{6+x}$ in the normal state.

Acknowledgements

The author gratefully acknowledges helpful discussions with H. Alloul, J. Bobroff, P. Bourges, C. Hammel, B. Keimer, Y. Sidis, and C.P. Slichter. The author also thanks H. Alloul and J. Bobroff for helpful comments on the manuscript and the Laboratoire de Physique des Solides at Orsay for

its hospitality. The numerical computations reported in this paper were performed at the Center for Information Technology at Koç University.

Appendix A. ^{7}Li Knight shift

In the presence of a uniform static magnetic field, $\mathbf{B} = B_0\mathbf{z}$, and a hyperfine coupling to the electronic spins given by Eq. (18), the interaction energy of a ^{7}Li nuclear moment $^7\mu = \hbar^7\gamma_n\mathbf{I}$ is

$$-\hbar^7\gamma_n I^z B_0 + CI^z \sum_{i=1}^{4} \langle S^z(\mathbf{r}_i)\rangle, \tag{A.1}$$

where i sums over the four Cu(2) sites neighboring the ^{7}Li impurity. This expression can be rewritten as

$$-\hbar^7\gamma_n I^z B_0(1 + {}^7K), \tag{A.2}$$

where the ^{7}Li Knight shift ^7K defined by

$${}^7K = -\left(\frac{C}{\hbar^7\gamma_n B_0}\right) \sum_{i=1}^{4} \langle S^z(\mathbf{r}_i)\rangle \tag{A.3}$$

gives the fractional change in the Zeeman frequency of the nuclear magnetic moment due to the hyperfine coupling. According to the Kubo linear-response theory [46], the expectation value at time t of the electronic spin at site $\mathbf{r}_i$, $\langle S^z(\mathbf{r}_i, t)\rangle$, is given by

$$\langle S^z(\mathbf{r}_i, t)\rangle = -i \int_{-\infty}^{t} \mathrm{d}t' \langle [S^z(\mathbf{r}_i, t), V_Z(t')]\rangle \theta(t - t'), \tag{A.4}$$

where $V_Z(t') = \mathrm{e}^{\mathrm{i}H_0 t} V_Z \mathrm{e}^{-\mathrm{i}H_0 t}$ with the Zeeman term for the electronic spins

$$V_Z = -\hbar\gamma_e B_0 \sum_j S^z(\mathbf{r}_j). \tag{A.5}$$

In Eq. (A.4), the expectation values are evaluated with respect to the eigenstates of

$$H_0 = H_{\mathrm{Hubbard}} + V_{\mathrm{imp}}, \tag{A.6}$$

where H_{Hubbard} is given by Eq. (1) and the impurity interaction V_{imp} is given by Eq. (9). In the adiabatic limit and as $t \to \infty$, $\langle S^z(\mathbf{r}_i)\rangle$ is related to the magnetic susceptibility [46], and in this limit Eq. (A.4) reduces to

$$\langle S^z(\mathbf{r}_i)\rangle = \frac{1}{2}\hbar\gamma_e B_0 \sum_j \chi(\mathbf{r}_i, \mathbf{r}_j) \tag{A.7}$$

where the transverse susceptibility $\chi(\mathbf{r}_i, \mathbf{r}_j) = \chi(\mathbf{r}_i, \mathbf{r}_j, \mathrm{i}\omega_m = 0)$ is defined by Eq. (15). Hence, the ^{7}Li Knight shift is given by

$${}^7K = \frac{1}{2}\left(\frac{\gamma_e}{{}^7\gamma_n}\right) C \sum_{i=1}^{4} k(\mathbf{r}_i) \tag{A.8}$$

where

$$k(\mathbf{r}_i) = \sum_j \chi(\mathbf{r}_i, \mathbf{r}_j) \tag{A.9}$$

with j summing over the whole lattice. Note that for the pure system $k(\mathbf{r}_i)$ reduces to $\chi_{\mathrm{pure}}(\mathbf{q} \to 0)$.

Appendix B. V_{eff} at lowest order in U

It is possible that the effective impurity potential has an extended component because of the correlated nature of the host material [28]. At lowest order in the bare impurity potential V_0 and the Coulomb repulsion U, such a contribution originates from the scattering process shown in Fig. 15.

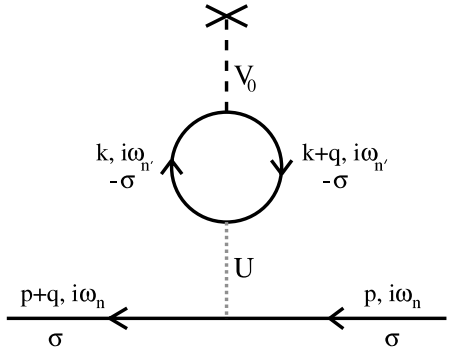

Fig. 15. Feynman diagram for a scattering process which causes the effective impurity potential to be extended in real space. This diagram is lowest order in U and the bare impurity potential V_0. Here, an electron with momentum $\mathbf{p}$, Matsubara frequency ω_n and spin σ scatters to a state with momentum $\mathbf{p} + \mathbf{q}$, Matsubara frequency ω_n and spin σ.

This process leads to a momentum-dependent effective interaction which is given by

$$V_{\rm eff}^{(1)}(\mathbf{q}) = -V_0 U \chi_0^{\rm L}(\mathbf{q}), \tag{B.1}$$

where $\chi_0^{\rm L}$ is the Lindhard susceptibility of the pure system, Eq. (5). Since $\chi_0^{\rm L}(\mathbf{q})$ peaks at $\mathbf{q} \sim (\pi,\pi)$, $V_{\rm eff}^{(1)}$ is attractive at sites neighboring the impurity when $V_0 < 0$. For large V_0, it is necessary to replace the bare impurity potential in Fig. 15 by the impurity scattering t-matrix, in which case one obtains

$$V_{\rm eff}^{(1)}(\mathbf{q}) = U\frac{T}{N}\sum_{\mathbf{k},{\rm i}\omega_{n'}} G_0(\mathbf{k},{\rm i}\omega_{n'})G_0(\mathbf{k}+\mathbf{q},{\rm i}\omega_{n'}) \times \frac{V_0}{1 - V_0 F_0({\rm i}\omega_{n'})}, \tag{B.2}$$

where

$$F_0({\rm i}\omega_n) = \frac{1}{N}\sum_{\mathbf{p}} G_0(\mathbf{p},{\rm i}\omega_n). \tag{B.3}$$

The Fourier transform

$$V_{\rm eff}^{(1)}(\mathbf{r}) = \frac{1}{N}\sum_{\mathbf{q}} {\rm e}^{{\rm i}\mathbf{q}\cdot\mathbf{r}} V_{\rm eff}^{(1)}(\mathbf{q}) \tag{B.4}$$

gives the real-space structure of the effective interaction. This calculation of $V_{\rm eff}^{(1)}(\mathbf{r})$ has been carried out for $V_0 = -100t$, $T = 100$ K and $W = 3$ eV, and it is found that $V_{\rm eff}^{(1)}(\mathbf{r})$ at $\mathbf{r} = (1,0)$ is $-0.017t$. Even though $V_{\rm eff}^{(1)}(\mathbf{r} = (1,0))$ is found to be attractive in leading order in U, its magnitude is smaller by a factor of three from $V_1 = -0.05t$ found by fitting the ^7K data on optimally doped $YBa_2Cu_3O_{6+x}$.

This is the behavior expected for $V_{\rm eff}$ at lowest order in U. Clearly, an approximation which is first order in U would be insufficient. The actual structure of $V_{\rm eff}$, which includes scattering processes to all orders in U, depends on the reducible particle–particle vertex in the singlet and the triplet channels. Hence, it would be useful to calculate $V_{\rm eff}$ using exact numerical techniques in the paramagnetic state of the Hubbard or the t–J models. However, it should be noted that the structure in the electron density $n(\mathbf{r})$ does not necessarily reflect the structure in $V_{\rm eff}$, as it was seen in Fig. 11(c). In Ref. [28], $V_{\rm eff}$ was calculated for the t–J model but at half-filling, where $V_{\rm eff}$ at the $(1,0)$ site was found to be repulsive. However, the insulating state might be different than the paramagnetic state, which is considered here. In Ref. [21], an effective impurity interaction which is repulsive at $\mathbf{r} = (1,0)$ was used for calculating the enhancement of the uniform susceptibility by dilute nonmagnetic impurities. Since both positive and negative values of V_1 act to enhance the uniform susceptibility, this does not determine the sign of V_1. On the other hand, the Knight shift data studied here require that, at the level of RPA, $V_{\rm eff}$ at the nearest-neighbor sites of the impurity is weakly attractive.

References

[1] A.V. Mahajan, H. Alloul, G. Collin, J.-F. Marucco, Phys. Rev. Lett. 72 (1994) 3100.

[2] J. Bobroff, W.A. MacFarlane, H. Alloul, P. Mendels, N. Blanchard, G. Collin, J.-F. Marucco, Phys. Rev. Lett. 83 (1999) 4381.

[3] P. Mendels, J. Bobroff, G. Collin, H. Alloul, M. Gabay, J.-F. Marucco, N. Blanchard, B. Grenier, Europhys. Lett. 46 (1999) 678.

[4] A.V. Mahajan, H. Alloul, G. Collin, J.-F. Marucco, Eur. Phys. J. B 13 (2000) 457.

[5] H. Alloul, J. Bobroff, A. Mahajan, P. Mendels, Y. Yoshinari, J. Phys. Soc. Jpn., Suppl. B 59 (2000) 114.

[6] W.A. MacFarlane, J. Bobroff, H. Alloul, P. Mendels, N. Blanchard, G. Collin, J.-F. Marucco, Phys. Rev. Lett. 85 (2000) 1108.

[7] M.-H. Julien, T. Feher, M. Horvatic, C. Berthier, O.N. Bakharev, P. Segransan, G. Collin, J.-F. Marucco, Phys. Rev. Lett. 84 (2000) 3422.

[8] K. Ishida, Y. Kitaoka, N. Ogata, T. Kamino, K. Asayama, J.R. Cooper, N. Athanassopoulou, J. Phys. Soc. Jpn. 62 (1993) 2803.

[9] G. Zheng, T. Odaguchi, T. Mito, Y. Kitaoka, K. Asayama, Y. Kodama, J. Phys. Soc. Jpn. 62 (1993) 2591.

[10] K. Ishida, Y. Kitaoka, K. Yamazoe, K. Asayama, Y. Yamada, Phys. Rev. Lett. 76 (1996) 531.

[11] K. Kakurai, S. Shamoto, T. Kiyokura, M. Sato, J.M. Tranquada, G. Shirane, Phys. Rev. B 48 (1993) 3485.

[12] Y. Sidis, P. Bourges, B. Hennion, L.P. Regnault, R. Vielleneuve, G. Collin, J.F. Marucco, Phys. Rev. B 53 (1996) 6811.

[13] H.F. Fong, P. Bourges, Y. Sidis, L.P. Regnault, J. Bossy, A. Ivanov, D.L. Milius, I.A. Aksay, B. Keimer, Phys. Rev. Lett. 82 (1999) 1939.

[14] Y. Sidis, P. Bourges, B. Keimer, L.P. Regnault, J. Bossy, A. Ivanov, B. Hennion, P. Gautier-Picard, G. Collin, preprint, cond-mat/0006265.

[15] N. Bulut, D. Hone, D.J. Scalapino, E.Y. Loh, Phys. Rev. Lett. 62 (1989) 2192.
[16] A. Sandvik, E. Dagotto, D.J. Scalapino, Phys. Rev. B 56 (1997) 11701.
[17] D. Poilblanc, D.J. Scalapino, W. Hanke, Phys. Rev. Lett. 72 (1994) 884.
[18] D. Poilblanc, D.J. Scalapino, W. Hanke, Phys. Rev. B 50 (1994) 13020.
[19] M. Gabay, Physica C 235–240 (1994) 1337.
[20] J.-X. Li, W.-G. Yin, C.-D. Gong, Phys. Rev. B 58 (1998) 2895.
[21] N. Bulut, Phys. Rev. B 61 (2000) 9051.
[22] N. Bulut, Physica C 353 (2001) 270.
[23] C.H. Pennington, C.P. Slichter, Phys. Rev. Lett. 66 (1991) 381.
[24] Y. Itoh, H. Yasuoka, Y. Fujiwara, Y. Ueda, T. Machi, I. Tomeno, K. Tai, N. Koshizuka, S. Tanaka, J. Phys. Soc. Jpn. 61 (1992) 1287.
[25] T. Imai, C.P. Slichter, A.P. Paulikas, B. Veal, Phys. Rev. B 47 (1993) 9158.
[26] M. Takigawa, Phys. Rev. B 49 (1994) 4158.
[27] T. Xiang, J.M. Wheatley, Phys. Rev. B 51 (1995) 11721.
[28] W. Ziegler, D. Poilblanc, R. Preuss, W. Hanke, D.J. Scalapino, Phys. Rev. B 53 (1996) 8704.
[29] L.S. Borkowski, P.J. Hirschfeld, Phys. Rev. B 49 (1994) 15404.
[30] N. Bulut, D. Hone, D.J. Scalapino, N.E. Bickers, Phys. Rev. Lett. 64 (1990) 2723.
[31] N. Bulut, D.J. Scalapino, Phys. Rev. Lett. 67 (1991) 2898.
[32] N. Bulut, D.J. Scalapino, S.R. White, Physica C 246 (1995) 85.
[33] F. Mila, T.M. Rice, Physica C 157 (1989) 561.
[34] M. Arai, T. Nishijima, Y. Endoh, T. Egami, S. Tajima, K. Tomimoto, Y. Shiohara, M. Takahashi, A. Garrett, S.M. Bennington, Phys. Rev. Lett. 83 (1999) 608.
[35] Ph. Bourges, B. Keimer, L.P. Regnault, Y. Sidis, preprint, cond-mat/0006085.
[36] F. Rullier-Albenque, P.A. Vieillefond, H. Alloul, A.W. Tyler, P. Lejay, J.F. Marucco, Europhys. Lett. 50 (1) (2000) 81.
[37] J. Bobroff, H. Alloul, F. Rullier-Albenque, P.A. Vieillefond, Physica C 282–287 (2000) 1389.
[38] J.S. Langer, Phys. Rev. 120 (1960) 714.
[39] H. Alloul, T. Ohno, P. Mendels, Phys. Rev. Lett. 63 (1989) 1700.
[40] M. Takigawa, W.L. Hults, J.L. Smith, Phys. Rev. Lett. 71 (1993) 2650.
[41] N. Bulut, U. Yaz, unpublished.
[42] S.H. Pan, E.W. Hudson, K.M. Lang, H. Eisaki, S. Uchida, J.C. Davis, Nature 403 (2000) 746.
[43] Y. Sidis, private communication.
[44] J. Bobroff, H. Alloul, W.A. MacFarlane, P. Mendels, N. Blanchard, G. Collin, J.-F. Marucco, preprint, cond-mat/0010234.
[45] J. Haase, C.P. Slichter, R. Stern, C.T. Milling, D.G. Hinks, Third International Conference on Stripes and High T_c Superconductivity, Rome, 2000.
[46] G. Mahan, Many-Particle Physics, Plenum Press, New York, 1981.